Ceramics International 52 (2026) 17019–17033

Contents lists available at ScienceDirect

Ceramics International

journal homepage: www.elsevier.com/locate/ceramint

Impact of yttrium doped on $15Na_2O•xY_2O_3•(17\text{-}x)P_2O_5•59.5V_2O_5•8.5Fe_2O_3$ glass and glass-ceramics as cathode for Na-ion batteries

A. Shreif [a,*], Y. Arita [a], Z. Homonnay [b], E. Kuzmann [b], M. Kudor [b], K.A. Beres [b,c], S. Krehula [d], M. Marciuš [d], L. Pavić [d], A. Šantić [d], M. Razum [d], S. Kubuki [a]

[a] Graduate School of Science, Tokyo Metropolitan University, 1-1 Minami-Osawa, Hachi-Oji, 1920397, Tokyo, Japan
[b] Institute of Chemistry,ELTE Eötvös Loránd University, Pázmány Péter Sétány 1/A, 1117, Budapest, Hungary
[c] Institute of Materials and Environmental Chemistry, HUN-REN Research Centre for Natural Sciences, H-1117, Budapest, Hungary
[d] Division of Materials Chemistry, Ruđer Bošković Institute, Bijenička 54, Zagreb, 10000, Croatia

ARTICLE INFO

Keywords:
SIB
Cathode materials
Non-bridging oxygen
Mössbauer spectroscopy
XAFS
Electrochemical

ABSTRACT

Rising cost and limited availability of lithium present major challenges for the scalability of lithium-ion batteries. These constraints have motivated the researcher to seek alternative solutions, with sodium emerging as a promising candidate because of its abundance and low cost. Therefore, sodium-ion batteries (SIB) are receiving a lot of attention which has driven researchers to further develop and improve of SIBs. In this present study, we selected the iron-vanadium-phosphate glass ceramics as a base because its promising cathode for sodium ion battery, and were doped with Yttrium to enhance their performance. Glass samples with the composition $15Na_2O•xY_2O_3•(17\text{-}x)P_2O_5•V_2O_5•8.5Fe_2O_3$, where ($x$ = 1, 3, 5 mol%), were prepared by the melt quenching method. Before and after heat-treat ted *x*YNPVF samples, respectively denoted as BHT- and AHT-*x*YNPVF were characterized by Differential thermal analysis (DTA), X-ray diffraction (XRD), Fourier transform infrared spectroscopy (FTIR), X-ray absorption fine structure (XAFS), ^{57}Fe-Mössbauer spectra (FeMS), impedance spectroscopy, and charge-discharge capacity in SIB. The XRD patterns of AHT-*x*YNPVF presence of the three crystalline phases YPO_4 and $NaVP_2O_7$, and $Na_{0.282}V_2O_5$ after heat treatment. FTIR spectra of BHT- and AHT-*x*YNPVF reveal that Y_2O_3 enters as a modifier in the glass network, leading to an increase in non-bridging oxygen. The results of ^{57}Fe-Mössbauer spectra and XANES of BHT- and AHT-*x*YNPVF showed that iron existed as Fe^{3+} with the octahedral coordination. Impedance spectroscopy revealed that the DC conductivity of BHT-*x*YNPVF glasses increases with increasing Y_2O_3 content and with additional heat treatment. Charge-discharge capacity shows that the highest initial capacity was 57.4 mAh g^{-1} for the AHT-1YPVFN at a current density of 50 mA g^{-1}, and increased to 210 mAh g^{-1} at a current density of 5 mA g^{-1}. It is concluded that the introduction of Y_2O_3 into sodium phosphor vanadate glass resulted in an increase in the cathode performances in SIB.

1. Introduction

Producing energy from fossil fuels represents one of the world's greatest challenges, owing to the enhanced greenhouse effect caused by the carbon dioxide emissions inherent to their use. To address this issue, it is imperative to reduce our dependence on fossil-fuel-based power generation and to seek alternative, environmentally benign solutions that mitigate such pollution and, consequently, curb global warming [1–4]. Accordingly, harnessing solar, wind, and other forms of renewable energy has become an essential solution to reduce this problem. Although initial production costs were exceedingly high, sustained research and development efforts have reduced costs to only 1.5 to 3 times those of conventional fossil-fuel generation [5].

Advancing battery technology and increasing storage capacity are both essential to the widespread adoption of renewable energy. Lithium-ion batteries have emerged as a “magic solution” in this domain, owing to their high storage capacity and substantial voltage differential, which together yield considerable electrical power. Nevertheless, the relative scarcity of lithium in the Earth's crust drives up production costs and raises concerns regarding its long-term availability should reliance on it

* Corresponding author.
E-mail addresses: a.shreif1995@azhar.edu.eg, ahmed-hanafy@ed.tmu.ac.jp (A. Shreif).

https://doi.org/10.1016/j.ceramint.2026.02.289
Received 1 January 2026; Received in revised form 12 February 2026; Accepted 17 February 2026
Available online 19 February 2026
0272-8842/© 2026 The Authors. Published by Elsevier Ltd. This is an open access article under the CC BY license (http://creativecommons.org/licenses/by/4.0/).

become predominant [6–8]. To alleviate this prospective crisis, scientists and researchers have identified sodium as an optimal alternative element. Sodium is far more abundant in the Earth's crust than lithium and incurs lower production costs, operates on the same fundamental electrochemical principles, also exhibiting a standard electrode potential of −2.7 V. A typical battery comprises three principal components: cathode, anode, and electrolyte. The cathode is regarded as the bottleneck in battery performance, as it plays a key role in determining the overall cell voltage, energy density, and cycle life. Consequently, enhancing cathode properties is critically important [9,10].

A wide range of conventional cathodes, including layered transition-metal oxides, tunnel- and spinel-type oxides, olivine phosphates and silicates, metal hexacyanoferrates, fluorides, and polyanionic compounds, have been extensively investigated. However, these materials commonly suffer from limited specific capacity, poor ionic and electronic conductivity, structural instability during repeated charge–discharge cycles, and undesirable side reactions with electrolytes, which significantly restrict their practical application. Glass and glass-ceramic cathodes have recently emerged as promising alternatives due to their open two- and three-dimensional framework structures, superior electrochemical and mechanical stability, and enhanced Na^+-ion diffusion. These characteristics enable improved cycling performance, safety, and compatibility, making glass and glass-ceramic materials attractive candidates for cathode for sodium-ion batteries [10–13].

Among cathode candidates, mixed polyanion glass materials have shown promise by combining transition-metal redox activity with versatile glass networks. Sodium- Phosphate–vanadate–iron (NPVF) glasses. In this composition, the phosphate component enhances structural support due to its ability to form strong covalent bonds with oxygen atoms. It also acts as a reducing agent, increasing the reduction levels of vanadium and iron. This, in turn, promotes redox activity, which ultimately leads to an increase Oxidation-reduction process, which forms the fundamental scientific basis of batteries. Early studies demonstrated that introducing V_2O_5 into iron phosphate glasses dramatically enhances Na^+ intercalation: for example, substituting vanadate for phosphate raised the Fe-P glass capacity from near zero to the full theoretical value [11]. Likewise, recent work on Sodium–Phospho–Vanadate glasses (xNa_2O-$10P_2O_5$-(90-x) V_2O_5) reported large initial capacities (~184 mAh g^{-1} for 25 mol%Na_2O at the current density is 0.2 mA cm^{-2}) for Sodium-Ion Battery SIB [14]. Rui et al. successfully developed a novel $Na_3V_3(PO_4)_4$ compound featuring a layered architecture that incorporates interconnected 3D sodium-ion pathways. This unique structural design enables the material to deliver special cycling stability and rate capability. Remarkably, the material maintains outstanding electrochemical performance even when subjected to high current densities up to 3C. Additionally, the initial capacity is 37 mAh g^{-1} for 67.5 mA g^{-1} [15].

Rare-earth oxide dopants have long been used to modify oxide glass networks and improve performance. Yttrium oxide (Y_2O_3) in particular is a high-field-strength additive that tends to enter glass networks as YO_6 polyhedral. In phosphate glasses, Y^{3+} preferentially bonds to non-bridging oxygens (terminal O of PO_4) and acts as a network modifier. Solid-state NMR and spectroscopic studies report that Y_2O_3 addition depolymerizes the phosphate chain network: metaphosphate (Q^2) species decrease while pyrophosphate (Q^1) units increase with Y content [16]. For example, in sodium-containing glasses, Y doping can also affect Na^+ transport. For instance, sodium-yttrium silicate glasses have shown excellent Na^+ conductivities (10^{-8} S/cm at 25 °C, rising to ~10^{-3} S/cm at 300 °C) [17]. Introducing Y_2O_3 could perturb the structure: for example, Y-O-P linkages might compete with V-O-P connectivity or distort the V=O environment, which may lead to increasing the oxidation-redox processing. While Y^{3+} does not provide additional redox capacity, similar strategies in oxide cathodes have shown that high-valence cations can stabilize lattice oxygen and modify charge distribution [18]. Ning et al. improvement of the cycling performance and rate capability by preparing lithium-rich cathode material for LIB by using $Li_{1.2}Mn_{0.6-x}Ni_{0.2}Y_xO_2$ ($0<x<0{,}05$) by an oxalate co-precipitation method where that addition the Y^{3+} to the material can expand Li^+ diffusion channels in layered structure and improvement the stabilized material structural and give high capacity retention 240 $mAhg^{-1}$ after 40 cycle at 0.1C rate and superior rate capability 184.5 $mAhg^{-1}$after 40 cycle at the rate 1C [19]. $LiNi_{0.8}Co_{0.1}Al_{0.05}O_2$, abbreviation as NCA has a lot of attention because of its high voltage, specific energy, and specific capacity, but the stability of NCA is still a big challenge. Sharziket et al. succeeded in doping the Y^{3+} and Na^+ in the structure to improve the thermal and structural stability of NCA to be used as a cathode for SIB. The best result was shown in the sample 0.5 Na-0.5Y-NCA, where a given discharge capacity of 161.23 mAh g^{-1} after 100 cycles at a rate of 0.5C with a capacity retention of 94% [20]. Junming et al. found that the small amount of Y^{3+} kept the microstructure of $LiFePO_4$/C and modified the particle morphology, which improves the electrochemical performance of $LiFfePO_4$/C, where $LiFe_{0.98}Y_{0.02}PO_4$/C shows the best discharge capacity 119.6 mAh g^{-1} after 100 cycles at 5C, with a capacity retention 85.5 % [21].

Literature reports indicate that NPVF glass and glass ceramics could be a good choice for application as a cathode for SIB. Additionally, the Y_2O_3 enhances cycle stability due to its electronic structure, which also contributes to improved charge capacity. Accordingly, in this study, the incorporation of Y_2O_3 into NPVF glass is expected to improve both cycle stability and discharge capacity.

2. Preparation and characterization

2.1. Preparation xYNPVF

Glass samples with the $15Na_2O•xY_2O_3•(17\text{-}x)P_2O_5•V_2O_5•8.5Fe_2O_3$, where ($x$ = 1, 3, 5 mol%), denoted as xYNPVF, were prepared by the melt quenching method. Chemical reagents of V_2O_5 (226-00125, Wako), $NH_4H_2PO_4$ (012-03305, Wako), Fe_2O_3 (096-04825, Wako), Na_2CO_3 (196-01595, Wako), and Y_2O_3 (250-00442, Wako) were ground with each other in mortar to form homogeneous mixture. The mixture was then transferred into a platinum crucible and melted in an electric furnace (NHK-170, Nitto) at 900 °C for **90** min. The molten liquid was then rapidly quenched in ice water to form the glass samples. Subsequently, each glass sample was heat-treated at 500 °C for 100 min in the same furnace as shown in Fig. 1.

2.2. Characterization

The details of characterization are listed in the supporting information.

2.3. Solid-state impedance spectroscopy (ss-IS)

For electrical measurements, samples were prepared in pellets, ~0.8 mm thick, and Au electrodes, 3.8 mm in diameter, applying a consistent force of 2 × 10^3 kg *via* a hydraulic press. To establish electrical connections, gold electrodes, measuring 3.8 mm in diameter, were deposited on both sides of the disk pellets using a sputter coater SC7620 by Quorum Tech.

2.4. Preparation of sodium-ion battery

The cathode of the Na-ion battery was prepared using a mass ratio 70:25:5 for the glass ceramics sample, acetylene carbon black (ab, 99.99%, 06-0025, Strem Chemicals, USA): polytetrafluoroethylene (PTFE, 165-13412, Wako Pure Chem., Japan), respectively. The total mass of the mixture was 30 mg. First, the xYNPVF glass/glass-ceramics powder was mixture with acetylene carbon black according to the above ratio and mixed together using a centrifuge at 800 rpm for 30 min. Then, 5 % of PTFE was add to the mixture. The resulting cathode was shipped into a pellet with a diameter of 10 mm, fixed to a Ti mesh, and vacuum

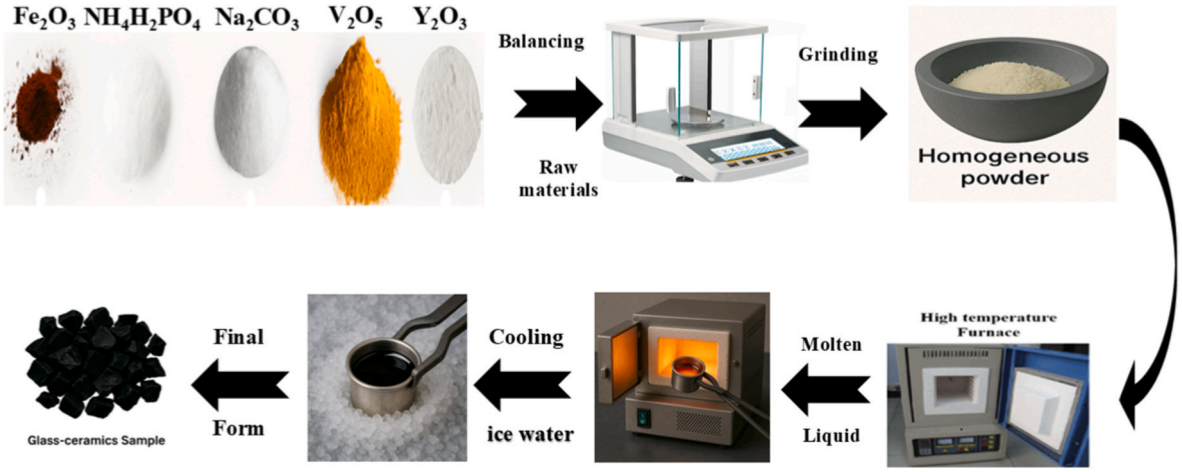

Fig. 1. Schematic of the preparation process for the *x*YPVFN glass samples *via* the melt-quenching technique.

dried at 110 °C for 24 h in a glass tube oven (GTO-200, Shibata Scientific Technologies, Japan) before cell assembling. After preparing the cathode, The CR2032 type coin cell was assembled using the cathode pellet, a separator (#3501, Celgard LLC, USA), an electrolyte of 1 M $NaClO_4$/ propylene carbonate (LIAPSTE-P/S1, Tomiyama Pure Chem., Japan) and the metallic Na anode (750-70852, Kishida, Japan). The anode was prepared using 90 mg metallic Na (750-70852, Kishida, Japan) with the same dimensions and fixed to Ni-mesh. All components of CR2032 were assembled in a glove box (DBO-1KP-MTK, Miwa Manufacturing Co., Ltd., Japan) under an O_2 concentration of less than 1.0 ppm. The charge-discharge capacity and cyclability of BHT -*x*YNPVF- and AHT-*x*YNPVF glass and glass-ceramics are measured at 25 °C varying a constant current density from 5, 25, 50, 100 and 200 mAg^{-1} in the voltage range from 0.8 to 4.1 V, using TOSCAT-3100SK, Toyo-System. The charge-discharge process was repeated for 30 cycles, with a rest period between charge and discharge of 10 min. Every sample has been measured 2 times to ensure the behavior (see Fig. 2).

3. Results and discussion

3.1. Differential thermal analysis DTA

Fig. 3 represents differential thermal analysis DTA thermograms for the prepared sample, whose composition is $15Na_2O•xY_2O_3•(17-x)P_2O_5•59.5V_2O_5•8.5Fe_2O_3$, where (*x* changes to 1, 3 and 5 mol %). The DTA curves confirm the amorphous phase for all sample preparations, where all samples exhibit an endothermic and an exothermic peak, which represent the glass transition temperature (T_g) and crystallization temperature (T_c), respectively.

After the T_g, two distinct exothermic peaks were observed for each sample, corresponding to crystallization temperature T_{c1}, T_{c2}. The endothermal peak shown after T_c represents the melting temperature T_m. The values of T_g, T_c, and T_m for all samples are listed in Table 1. As shown in Fig. 3 that the T_g, T_{c1}, and T_{c2} decrease when increasing the concentration of Y_2O_3. The factor T_g/T_m is used as an indicator for the glass stability, which is the ideal value being about 0.66 for stable glass [22].

The values of T_g/T_m for the *x*YNPVF glass with *x* of 1, 3 and 5 mol% are 0.44, 0.41, 0.39, respectively. The values of T_g/T_m are decreasing with concentration of Y_2O_3. Also observed that the T_{c1} decreases from

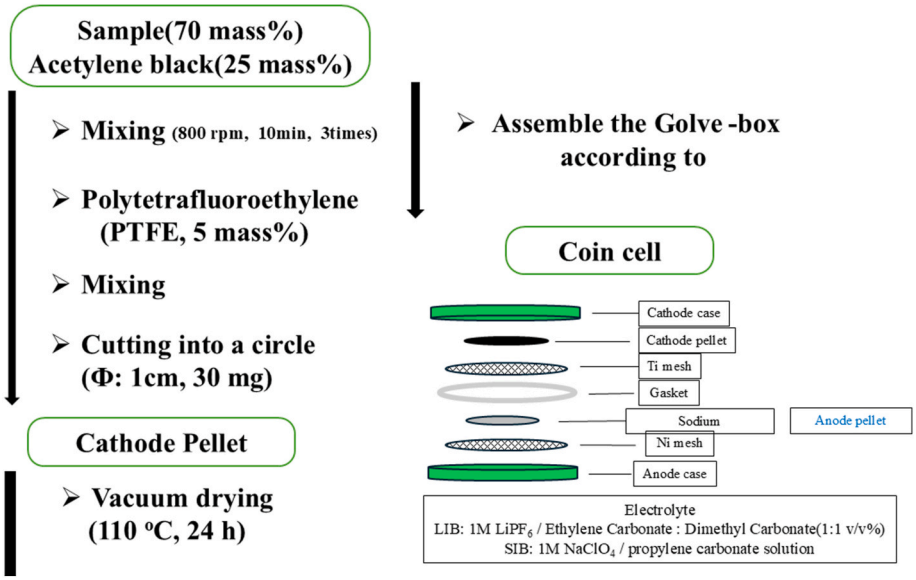

Fig. 2. Schematic diagram of CR 2023 type coin cell of Na-ion battery.

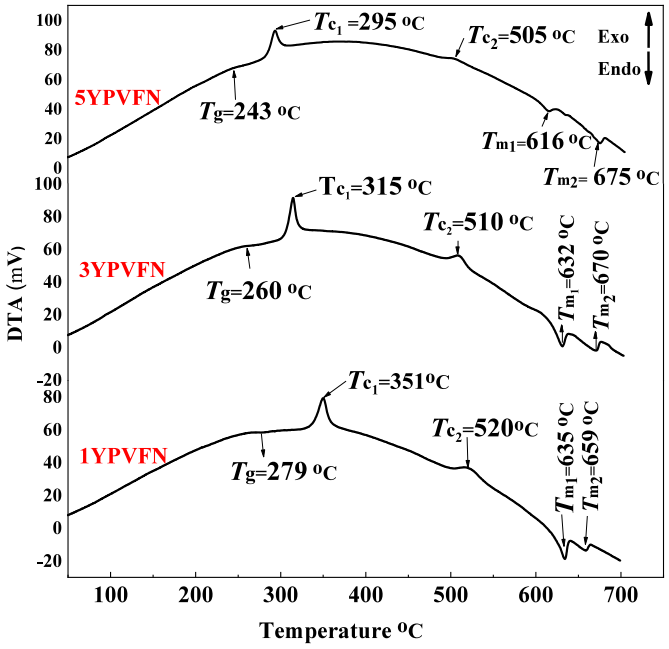

Fig. 3. DTA curves of *x*YNPVF with *x* of 1, 3 and 5 mol%.

Table 1
DTA parameter for all studied samples of YNPVF.

x/mol %	T_g/°C	T_{c1}/°C	T_{c2}/°C	T_{m1}/°C	T_{m2}/°C	T_g/T_m
1	279	351	520	635	659	0.44
3	260	315	510	632	670	0.41
5	243	295	505	616	675	0.39

351 °C to 295 °C, T_{c2} also decreases from 520 °C to 505 °C with increasing concentration of Y_2O_3. This progressive decrease suggests that incorporation of Y^{3+} promotes structural disorder and reduces thermal stability, which leads to crystallization at a lower temperature. This confirms that the Y^{3+} is introduced into the glass network as a modifier. when Y_2O_3 is added as a modifier, the Y^{3+} ion disrupts the bridging oxygen bond, such as P-O-P and V-O-V, and increases the concentration of NBOs. This leads to the glass becoming a more open and flexible structure. This process is known as depolymerization of the glass network, which explains why the increase in concentration of Y_2O_3 leads to a reduction in thermal stability [23].

3.2. The XRD pattern of xYNPVF

Fig. 4 shows the XRD pattern of BHT- and AHT-*x*YNPVF, respectively. The parameters obtained from the XRD of BHT- and AHT-*x*YNPVF are listed in Table 2. For BHT-*x*YNPVF, a broad hump is observed in the XRD patterns for $x = 1$, 3, and 5 mol% within the 2Θ range from 20° to 30° which indicates that the amorphous phases represented in all prepared samples. In addition, a sharp peak was observed at 2Θ = 25,85°, 35°, 51.95° in all prepared samples, indicating the presence of crystal phase. The intensity of this peak increases with Y_2O_3 content. Rietveld refinement of XRD patterns for xYNPVF showed that they belong to the crystalline phase YPO_4 (PDF NO 0.051353). Based on this result, the crystallite size was estimated by using the Scherrer equation [24] (see Fig. 5).

$$D = \frac{K\lambda}{\beta \cos(\theta)} \qquad \text{eq (1)}$$

where D is the crystallite size and k is a constant = 0.9, λ is the wavelength of the X-ray emitted from K_α Cu of 1.5xxx nm, and β full width at

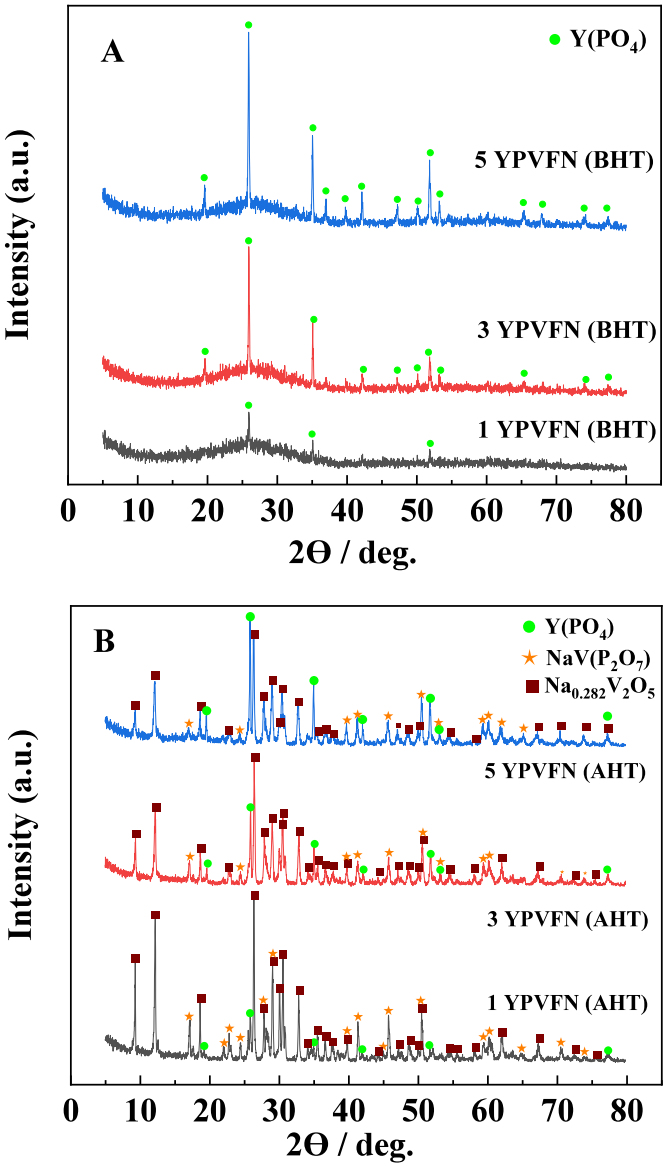

Fig. 4. XRD patterns of *x*YNPVF glass-ceramics (A) before and (B) after heat treatment.

half maximum of its X-ray diffraction peak. The crystallite size increases from 40 nm to 66.9 nm with the Y_2O_3 content, which confirms that all samples were prepared in a glass-ceramic nano-composition state. In contrast, the XRD pattern of AHT-*x*YNPVF in Fig. 4 (b) showed the new peaks with very sharp lines due to the heat treatment. By using the X-ray analyzer found that this sharp line belongs to three crystalline phases $Na_{0.282}V_2O_5$ (PDF No. 01-086-4171), $NaVP_2O_7$ (PDF No. 01-079-0740) and YPO_4 (PDF No. 0.051353). The phase of $Na_{0.0282}V_2O_5$ has great attention in the electrochemical application because of the flexibility of its structure in the intercalation/deintercalation processes, where sodium ions (Na^+) are situated within the structural tunnels, where they play a crucial role in maintaining structural integrity and preventing collapse. This transaction process is called “pillar effect” [25]. After calculation, it was shown that its crystallization size decreased with the increasing concentration of the Y_2O_3.

3.3. FTIR spectra

The pentavalent phosphate ion (PO_4^{3-}) typically shares three of its corners with neighboring tetrahedra through three bridging oxygen

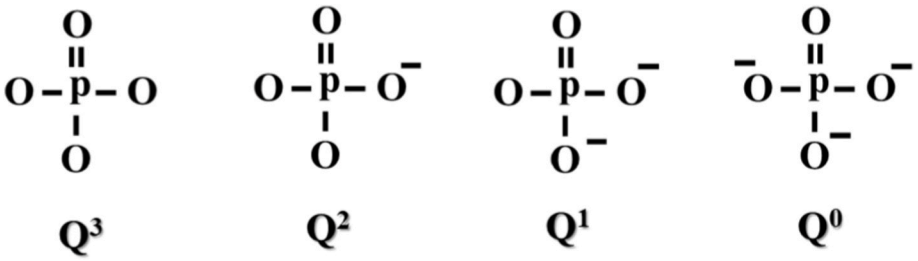

Fig. 5. Q. Site model.

Table 2
Crystalline phase, lattice parameter, space group, crystal structure, crystalline size for *x*YNPVF glass ceramics.

Sample		Crystalline phase	Lattice Parameters						Space Group	Crystal structure	Crystalite Size (nm)
BHT/AHT	*x* mol%		(Å)			(degree)					
			a	b	c	α	β	γ			
BHT	**1**	$Y(PO_4)$	6.88	6.88	6.01	90	90	90	$I4_1/amd$	Tetragonal	40
	3										69
	5										66.9
AHT	**1**	$Y(PO_4)$	6.88	6.88	6.01	90	90	90	$I4_1/amd$	Tetragonal	-
		$NaV(P_2O_7)$	7.32	7.92	9.58	90	111.96	90	$P12_1/c1$	Monoclinic	46.5
		$Na_{0.282}V_2O_5$	15.39	3.6	10.07	90	109.546	90	$C12/m1$	Monoclinic	58.8
	3	$Y(PO_4)$	6.88	6.88	6.01	90	90	90	$I4_1/amd$	Tetragonal	45.3
		$NaV(P_2O_7)$	7.37	7.98	9.65	90	111.96	90	$P12_1/c1$	Monoclinic	30
		$Na_{0.282}V_2O_5$	15.41	3.61	10.08	90	109.546	90	$C12/m1$	Monoclinic	56.8
	5	$Y(PO_4)$	6.88	6.88	6.01	90	90	90	$I4_1/amd$	Tetragonal	49.7
		$NaV(P_2O_7)$	7.33	7.93	9.59	90	111.96	90	$P12_1/c1$	Monoclinic	28.7
		$Na_{0.282}V_2O_5$	15.42	3.61	10.09	90	109.546	90	$C12/m1$	Monoclinic	56.4

atoms, leading to the formation of long chains, rings, or branched networks of interconnected PO_4 tetrahedra. The fourth oxygen atom usually remains bridge and does not participate in network connectivity. The Q. Site model suggested by Lippman et al. [26].

A structural model originally developed for binary silicate glasses, but for the first time has been applied to phosphate glasses; the possible reformation structure groups when addition alkaline oxide or the modifier oxide (M) is replace P-O-P bond by M-O-P bond that led to formation the single non bridging oxygen by increasing the ration of the modifier $R = MO/P_2O_5$ the consistencies of the chains P-O-P damage and the structure groups pass fromQ^3 to Q^2 to Q^1 to Q^0 at R equal to 0, 1, 2, 3 respectively [27].

Fig. 6 (a) shows the FTIR spectra for the prepared glass BHT-*x*YNPVF, where $x = 1$, 3 and 5. The spectra shows five broad peaks, 520, 820, 935, 1030, 1250 cm^{-1}, which mean overlapped peaks in the spectrum. So, to get better identification and more accurate information about structure using deconvolution (Gaussian function) to separate the overlapped peaks. The nine peaks show after deconvolution it the value of it is listed in Table 3 and shown in Fig. 6 (c). The peak in the range 1382-1429 cm^{-1} is representative to vibration of non-bridging oxygen PO_2 group that belong to Q^2 space [28] the band of the range 1225 to 1250 cm^{-1} is belong to the symmetric stretch of the P=O bond that belong to Q^2 space and it little movement to lower wavelength at introduced the Y^{3+} to the structure [29]. The bond 1080 cm^{-1} is attributed to the asymmetrical bending vibrations P-O-P [29]. The bond at 1030 to 1040 cm^{-1} is attached to the V=O isolated groups in the VO_5 trigonal bipyramids and the intensity increases as the concentration of the Y^{3+} increases [30] which enhances the existence of V^{5+} in the structure. The peak range 933 to 942 cm^{-1} is attributed to the stretching vibration of the P-O-P group, and notable that the intensity of the peak increases with the concentration of the Y^{3+} increasing, which means an enhancement of the existing bond in the structure of the BHT-*x*YNPVF [31]. The peak at 815 cm^{-1} is assigned to the stretching of V-O-V [30, 32]. The peak at 520 to 516 cm^{-1} is assigned to bond of Fe-O vibration mode (Fe^{3+}) for the octahedral and tetrahedral sites [33]. So it can be concluded that iron enters the structure as a former.

All the samples preparation BHT-*x*YNPVF exhibit FeO_4, PO_4 and VO_5 groups which led to form a 3-D structure, It is also noted that the increase of the concentration of the Y^{3+} led to increases the non-bridging oxygen which means that the Y^{3+} enter in structure as modifier as in agreement with the DTA result.

After the heat treatment, the new group formation depended on the change in the structure that happened from the treatment processing as noted in the X-ray. Fig. 6 (b) represents the spectrum of the AHT-*x*YNPVF, where $x = 1$, 3 and 5. As seen, there is an overlap peak shown in the spectrum, so after deconvolution, 19 peaks were found, listed in Table 4 and shown in Fig. 6(d). The peaks at range of 428 to 442 cm^{-1}, representative of the bending vibration of the O-P-O unit, which belongs to the Q^1 [34]. The peaks from 520 to 561 cm^{-1} is representative of the Fe-O bond in the FeO_4 tetrahedral structure, and the intensity of the peak increases when increasing the concentration of the Y^{3+} [32]. The peaks at 623 to 634 cm^{-1} is attributed to the bending vibration of the vanadium ion [35]. The peaks from 642 to 663 cm^{-1} represented the V-O-V antisymmetric stretching mode [28]. The peaks at range from 742 to 750 cm^{-1} is assigned to the symmetric vibration of the P-O-P bond, which belongs to Q^1 space [27]. The peaks observing in the range 851–870 cm^{-1} is attributed to the asymmetric stretching vibrations of V-O-P linkages, with possible contributions from non-bridging $P\text{-}O^-$ units [28,30]. The peak of the range 910 cm^{-1} represents the symmetric vibration PO_4^{-3} (PO) that belongs to Q^0 [31,36]. The peaks at the range 984 to 1110 cm^{-1} are representative of V=O in the VO_5 trigonal or V=O in V_2O_5 polyhedral [30,35]. The peaks observed in the range 1089 to 1114 cm^{-1} are assigned to the asymmetric stretching vibrations of P-O bonds in phosphate tetrahedra, corresponding mainly to Q^2 and Q^1 structural units [29,37]. The range of 1150 to 1175 cm^{-1} belongs to the P-O stretching mode, which belongs to Q^2 space [27]. The peak observed at 1207 corresponds to an asymmetrical stretch of the P=O bond, which belongs to Q^2 space [38]. The peak observed in the range 1315-1319 is assigned to asymmetric stretching vibration of terminal (P=O) or $\nu(PO_3)$ vibrations of terminal (non-bridging) phosphate units [29] The peaks

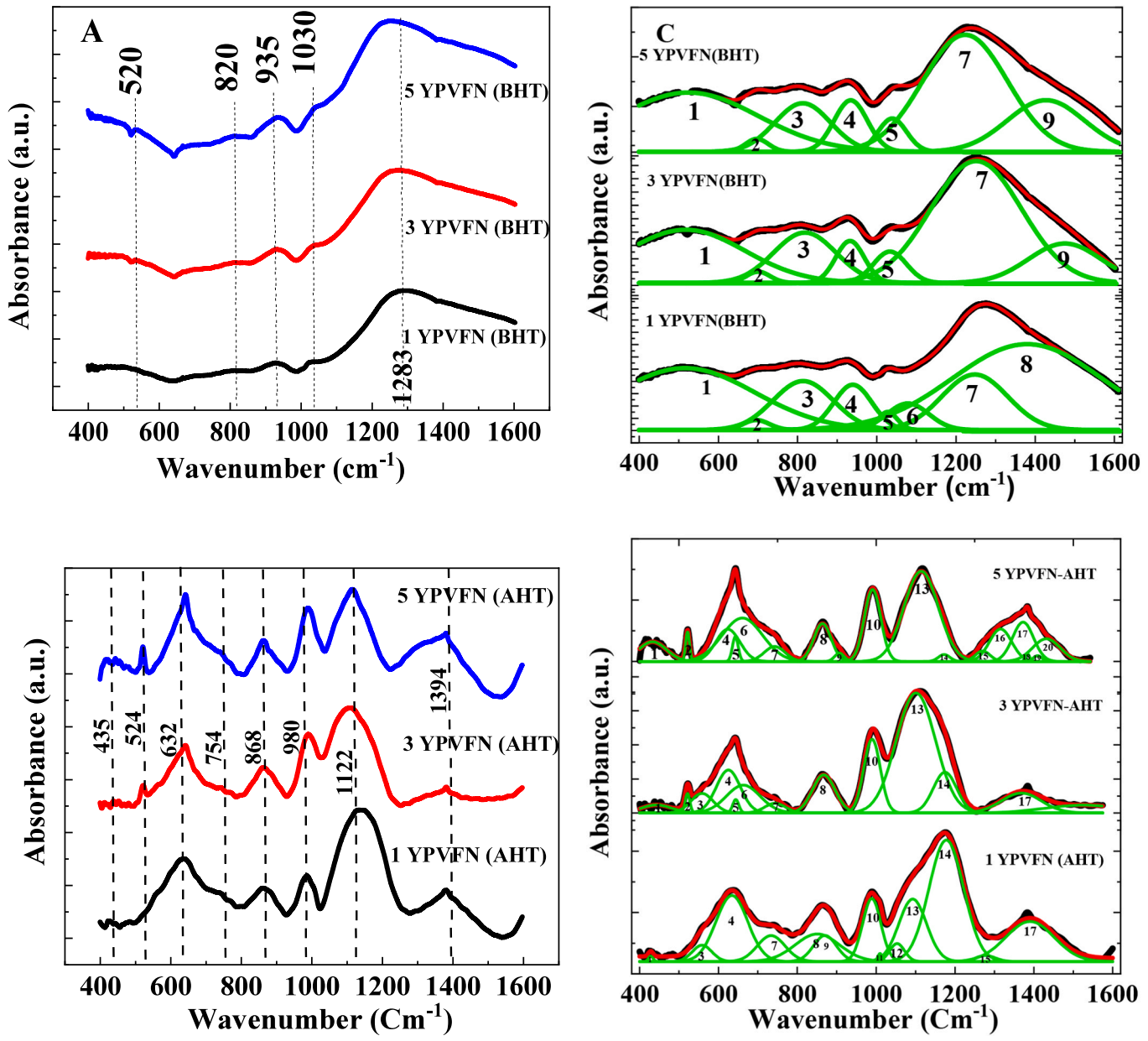

Fig. 6. FTIR and Deconvolution spectra of *x*YNPVF glass-ceramics with *x* of 1, 3 and 5, (A,C) before and (B,D) after heat treatment at 500 °C for 100 min.

Table 3
Assignment and Deconvolution parameters of the FTIR spectra of *x*YNPVF glass-ceramic for BHT.

Peak Number	BHT						Assignment
	1 YPVFN		3YPVFN		5 YPVFN		
	A %	ν cm^{-1}	*A* %	ν cm^{-1}	*A* %	ν cm^{-1}	
1	44.97	516	30.1	517	53.26	524	Fe-O stretching mode of $Fe(T_d)O_4$
2	1.366	696.6	1.291	701	1.906	698	V-O stretching mode of $V(T_d)O_4$
3	15.25	815.4	14.89	819	17.31	814	is associated with V-O-V stretching vibrations
4	8.963	941.1	5.742	933	11.07	935.8	the asymmetric vibration of P-O-P (Q^3)
5	1.801	1029	4.928	1035	6.099	1041	The V-O stretching mode of the VO_5 pyramid
6	5.712	1080	***	***	***	***	the asymmetrical bending vibrations P-OP(Q^2)
7	18.89	1250	52.88	1253	63.69	1225	The P-O stretching mode (Q^2)
8&9	66.02	1382	13.66	1478	25.68	1429	Vibrations of non-bridging (PO_2) groups (Q^2)

ν: band center (cm^{-1}), *A*: relative area (%). All spectra were recorded with a resolution of ±3 cm^{-1}.

from 1368 to 1430 cm^{-1} correspond to vibrations of non-bridging (PO_2) groups, where that PO_2 unit (O-P-O) belongs to Q^2 [28]. After heat treatment, a new bond add to the structure, and after assignment, it can be seen that the increase of Y_2O_3 enhances the existence of the non-bridging oxygen, which confirm that the Y^{3+} enter in the structure as modifier additionally the structure of the all sample *x*YNPVF connate

Table 4
Assignment and Deconvolution parameters of the FTIR spectra of *x*YNPVF glass-ceramic for AHT.

Peak Number	AHT						Assignment
	1 YPVFN		3YPVFN		5 YPVFN		
	ν cm^{-1}	*A* %	ν cm^{-1}	*A* %	ν cm^{-1}	*A* %	
1	428	1.35	443	1.76	433	4.07	Bending vibration of the O-P-O unit, which belongs to the Q^1
2	***	***	522	0.77	522	1.05	The Fe-O bond in the FeO_4 tetrahedral structure
3	558	2.16	558	3.7	***	***	
4	634	14.40	625	8.65	624	7.03	Bending vibration of the vanadium ion
5	***	***	643	0.7	643	1.3	The V-O-V antisymmetric stretching mode
6	***	***	663	7.9	661	15.9	
7	734	4.91	744	1.7	743	2.82	The symmetric vibration of the P-O-P bond, which belongs to Q^1 space
8	851	8.33	867	7.22	864	5.95	Asymmetric stretching vibrations of V-O-P linkages, with possible contributions from non-bridging $P-O^-$ units
9	870	4.07	***	***	907	0.72	The asymmetric vibration of P-O-P (Q^3)
10	989	7.87	990	10.21	991	10.73	Representative of V=O in the VO_5 trigonal or V=O in V_2O_5 polyhedral
11	1110	0.18	***	***	***	***	
12	1053	1.81	***	***	***	***	Asymmetric stretching vibrations of P-O bonds in phosphate tetrahedra, corresponding mainly to Q^2 and Q^1 structural units
13	1093	11.85	1101	39.3	1114	27.96	The P-O stretching mode, which belongs to Q^2 space
14	1178	28.73	1175	7.95	1172	0.72	Asymmetrical stretch of the P=O bond, which belongs to Q^2 space
15	1277	0.80	***	***	1270	1.4	asymmetric stretching vibration of terminal (P=O) or $\nu(PO_2)$ vibrations of terminal (non-bridging) phosphate units
16	***	***	***	***	1315	6.52	vibrations of non-bridging (PO_2) groups, where that PO_2 unit (O-P-O) belongs to Q^2
17	1389.88	13.28	1368	6.7	1372	7.43	
18	***	***	***	***	1384	0.3	
19	***	***	***	***	1409	0.46	
20	***	***	***	***	1432	5.63	

ν: band center (cm^{-1}), *A*: relative area (%). All spectra were recorded with the resolution of ± 3 cm^{-1}.

the FeO_4 and PO_4, VO_5 groups which mean that the all samples in 3-D structure.

3.4. XANES and EXAFS spectra

The X-ray absorption near-edge structure (XANES) analysis is specifically used to determine both the oxidation state and the coordination number of an element. This is achieved by analyzing two main regions in the spectrum: the pre-edge region and the normalization edge, owing to the sensitivity of this technique to the transitions occurring in the K shell. Density functional simulations show that the K-edge half-height in Fe_2O_3 (Fe^{3+}) is 2–3 eV higher than in Fe-O (Fe^{2+}), indicating that an increase in edge energy corresponds to an increase in the oxidation state [38b,39]. Fig. 7 (a, b) represents the XANES spectroscopy for the prepared glass ceramics of *x*YNPVF for BHT and AHT. Fe_3O_4 and Fe_2O_3 were used as standard materials in the Fe-K-edge spectrum. The normalized absorption of edge energy at the point of E = 0.5 is associated with the excitation of a 1s core electron to continuum states [40]. For Fe_3O_4 and Fe_2O_3 as standard material in the Fe-K-edge before and after heat treatment, the normalized absorption edge shows 7106.91, 7108.23 eV for before and 7107, 7108.44 eV for after heat treatment, respectively [39,40]. The position of normalization edge energy of all prepared samples of BHT- and AHT-*x*YNPVF states are higher than that of α- Fe_2O_3 (7107 eV) and Fe_3O_4 (7108.5 eV), where BHT-*x*YNPVF at 7109.21, 7109.26, 7109.31 eV, while AHT-*x*YNPVF at 7109.4, 7109.5, 7109.73 eV for $x = 1$, 3 and 5, respectively, which confirm essentially that the oxidation state of iron are Fe^{3+}. These findings are in agreement with the previously shown FTIR results and the consequently shown Mössbauer spectra [40].

The pre-edge peak referred to the quadruple transition from the 1s state to the 3d, although this transition is forbidden according to the selection rule, but it happens according to interference between the 4p and the 3d orbital, in what is known as hybridization [40,42]. The pre-absorption edge indicates that the iron existing in the environment has more covalent bonds and oxidation. The Fe pre-edge for Fe_2O_3 (hematite) shows a relatively weak pre-edge that's related to Fe^{3+} in octahedral sites, whereas Fe_3O_4 (magnetite, which has Fe^{3+} in tetrahedral sites and Fe^{2+}/Fe^{3+} in octahedral sites) exhibits a stronger pre-edge feature due to the presence of tetrahedrally coordinated Fe^{3+} [41]. The pre-edge energy peak at 7096 eV for reference material and its intensity

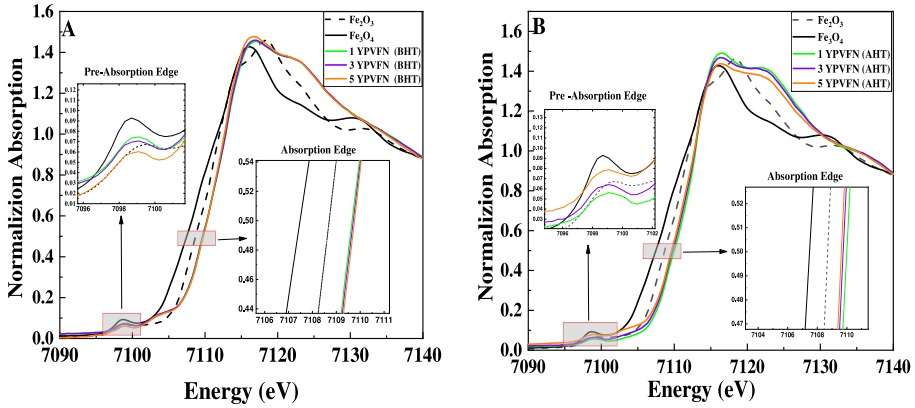

Fig. 7. Fe *K*-edge XANES spectra of *x*YNPVF glass-ceramics with *x* of 1, 3, and 5, (A) before and (B) after heat treatment at 500 °C for 100 min.

for Fe_3O_4, Fe_2O_3 are 0.092, 0.065, respectively, and for *x*YNPVF, decreasing from 0.073 to 0.059 for 1YPVFN, 5YPVFN-BHT, respectively. This led to the pre-edge peak becoming broader and closer to Fe_2O_3, which means that Fe^{3+} is largely in octahedral coordination but with some distortion or minor tetrahedral contribution [42]. For AHT, the pre-edge peak at 7096 eV for reference material and its intensity for Fe_3O_4, Fe_2O_3 are 0.092, 0.065, respectively, and for *x*YNPVF-AHT, an increase from 0.058 to 0.074 for AHT-1YPVFN, and 5YPVFN, respectively. It was also observed that the peaks become broader, and with increasing the concentration of Y_2O_3, the peak shifted to Fe_3O_4, which leads to the oxidation state is Fe^{3+}, and the coordination number tends to tetrahedral, with the existence of octahedral coordination. Therefore, from the result of the XANES for Fe-K edge, we can confirm that the Fe exists in the oxidation state Fe^{3+}, and the coordination number is predominantly octahedral with minor tetrahedral, in agreement with the results of Mössbauer and FTIR. It is well known that the post-edge range for the crystalline system of a normalized XANES spectrum does not fall below 1.0 [43,44]. However, in our samples, a reduction of the post-edge intensity below 1.0 is observed for both the before and after heat-treated states. This behaviour can be attributed to multiple scattering and/or resonance shape effects, which are commonly enhanced in glassy and glass-ceramic systems due to the lack of long-range crystalline order [45].

The FT-EXAFS of Fe-K edge spectra is used to determine the bond distance between the element and the coordination number from the peak position and intensity. As seen in Fig. 8, there is no change in the spectra of BHT and AHT-*x*YNPVF, which is in agreement with the XANES spectra. The spectrum of α-Fe_2O_3 is taken as a reference for analyzing the EXAFS spectrum of *x*YNPVF samples observed in Fig. 8(A) and (B), two peaks at 1.35 Å, 2.55 Å are detected, the first peak belongs to the Fe-O bond and the second peak belongs to the Fe-Fe [42]. BHT- and AHT-*x*YNPVF spectra with *x* of 1, 3 and 5 show the intense peaks at 1.46 Å, 1.48 Å. As it is observed, there is a shift to the higher bound between Fe and O due to the tendency to an octahedral structure. In the second peak region from 2 to 3.5 Å, no significant peaks in state BHT-*x*YNPVF and AHT-*x*YNPVF, which is attributed to structural distortion, in agreement with the XANES and Mössbauer spectra.

The normalization absorption for the V-K-edge representative in Fig. 9 for BHT- and AHT-*x*YNPVF, respectively, where the V_2O_5 representative is a standard material for the spectra of the prepared samples. The normalization absorption edge energy at the intensity of 0.5 showed at 5474.1 eV for the reference V_2O_5, for the sample BHT-*x*YNPVF at 5474.011, 5474.06 and 5474.1eV for $x = 1$, 3 and 5, while that of the heat-treated samples showed at 5474.34, 5474.17 and 5474.43 eV, respectively. Observed that all the samples prepared before and after heat treatment have a higher edge energy than the references, indicating that V^{5+} is the dominant oxidation state, and a little increase in the absorption edge enhancement the V^5 [42].

Observed that the pre-absorption edge for the V-K edge spectrum for the reference material V_2O_5 and for BHT-*x*YNPVF and AHT-*x*YNPVF is very high and sharp, which returns to the overlap that happens in the vanadium 3d and oxygen 2p orbitals [42]. The pre-edge appears as a small feature near 5460 eV for V_2O_5. With respect to BHT, and AHT--*x*YNPVF is no significant energy shift of the pre-absorption-edge peak, where the centroids remain up to 5458 eV. Whereas a decrease in oxidation number ($V^{5+} \rightarrow V^{4+}$) depends on the shift of the pre-edge to lower energy [41,47]. As can be seen from the normalized spectrum, the height of the pre-edge is similar in BHT- and AHT-*x*YNPVF, which suggests that the average coordination for Vanadium pyramidal, which leads to the coordination number, did not change dramatically during the annealing process, as confirmed by the XRD result.

Fig. 10 shows the FT-EXAFS of the V-K edge regarding the prepared glass *x*YNPVF-BHT and AHT respectively. The spectrum shows a different behavior in the BHT state compared to the AHT state. Considering BHT state, the spectrum of the V_2O_5 is taken as a reference for analyzing the EXAFS spectrum. Fig. 10(a) is divided into two parts. In the first part, two peaks are observed at 1.11 Å and 1.6 Å, corresponding to V-O bonds. In the second part, two peaks appear at 2.07 Å and 2.8 Å, attributed to V-V and V-M bonds, respectively, whereas M is another element [38c,46,48].

The *x*YNPVF-BHT spectrum, shows the first rang peak at 0.69 Å, 1.17 Å for $x = 1$ and 0.722 Å, 1.24 Å for $x = 3$, and 0.66 Å, 1.22 Å for $x = 5$ respectively, which indication that the V-O bond existing in the structure and for the second rang peak observed weak and broadening peak because the distortion structure of *x*YNPVF as result for this it is observed from Fig. 10 (a) there is shifted in the peak of the samples to the lower length bound between V and O that led to a higher oxidation state of vanadium (e.g. V^{5+}) and increasing the disorder of structure [49, 50] in the agreement with XANES results.

Regarding *x*YNPVF-AHT spectrum that shown in Fig. 10 (b) observed the first rang peak at 1.11 Å, 1.6 Å for $x = 1$ and 1.13 Å, 1.59 Å for $x = 3$, and 1.13 Å, 1.61 Å for $x = 5$ respectively, which indication that the V-O bond existing in the structure and for the second rang peak observed peak 2.05 Å, 2.68 Å for $x = 1$ and 2.05 Å, 2.66 Å for $x = 3$ and 2.03 Å, 2.66 Å for $x = 5$ respectively, which mean exist of V-V and V-P bond this happen because increasing in the ordinary of the structure in agreement with the X-ray [49]. As it is observed from Fig. 10 (b) there is a slight shift to the higher bound between V and O and high intensity of the peaks when the concentration of Y_2O_3 increases, which is referred to increasing in the coordination number, which is consistent with the

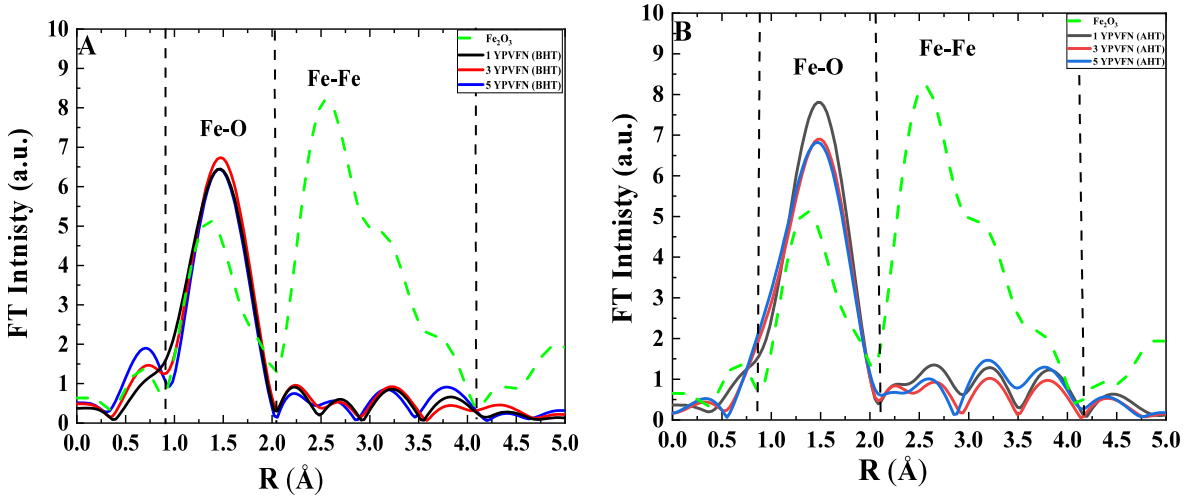

Fig. 8. Fourier transform of Fe *K*-edge EXAFS of *x*YPVFN glass-ceramics with *x* of 1, 3, and 5, (A) before and (B) after heat treatment at 500 °C for 100 min.

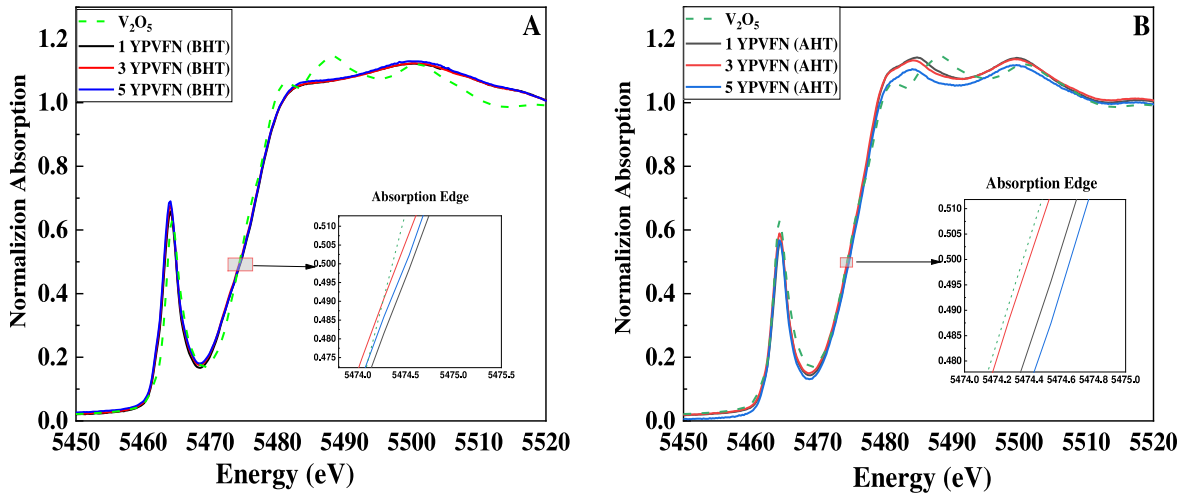

Fig. 9. V *K*-edge XANES spectra of *x*YPVFN glass-ceramics with *x* of 1, 3 and 5, (A) before and (B) after heat treatment at 500 °C for 100 min.

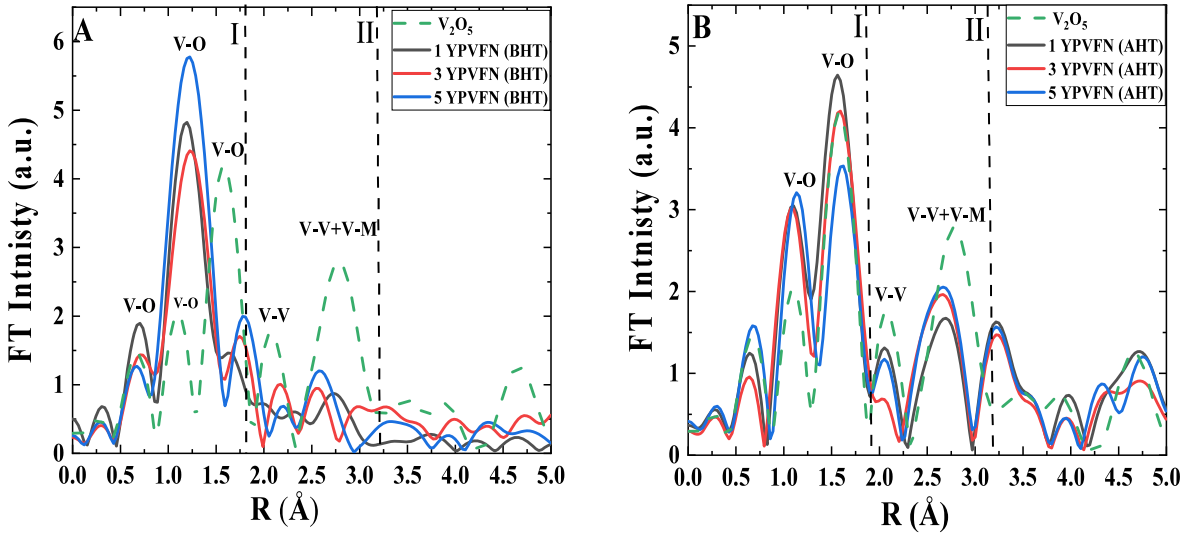

Fig. 10. Fourier transform of V *K*-edge EXAFS of *x*YPVFN glass-ceramics with *x* of 1, 3 and 5, (A) before and (B) after heat treatment at 500 °C for 100 min.

XANES results, indicating the dominance and increase of V^{5+} [50].

In the second range peak at ~2.66 Å was observed reduction in intensity and a shift to a lower distance bond. The shift to the lower distance bond happens because of the increase in the interaction between the vanadium and the neighboring atoms and the decrease in the intensity of the peak due to a decrease in the coordination number [50]. This is in agreement with the X-ray diffraction, where that may be explanation may exist the phase of $NaVP_2O_7$, despite the dominance of V^{5+} in the structure.

3.5. ^{57}Fe Mössbauer spectroscopy of xYNPVF

^{57}Fe Mössbauer spectroscopy is used to determine the fine structure of material by determining the interaction of the environment and the coordination state of the Fe atoms. The Fe^{3+} ions have two coordination numbers, Tetrahedral (T_d) and octahedral (O_h), The criterion values of the isomer shift for $Fe^{3+}(T_d)$ and $Fe^{3+}(O_h)$ was reported as $Fe^{3+}(T_d) < \delta = 0.3\text{-}0.41 < Fe^{3+}(O_h)$ with respect to alpha Fe [51]. Mössbauer parameters, isomer shift (δ), and quadrupole splitting (Δ) are related to the electron density and symmetry of charge distribution around the Fe nucleus. Fig. 11(a and b) represent the Mössbauer spectroscopy for *x*YNPVF-BHT and *x*YNPVF-AHT, measured at room temperature. Notably that the doublet peaks are represented in the BHT spectra.

The Mössbauer spectrum of BHT is shown in Fig. 11 (a) and the value of the parameter list is in Table 5. Notably that the isomer shift decreases from $0.42_{\pm 0.01}$ to $0.39_{\pm 0.01}$ mm s^{-1}, and the quadrupole splitting decreases from $0.72_{\pm 0.01}$ to $0.65_{\pm 0.01}$ mm s^{-1} when increasing the concentration of Y_2O_3. From the value of the isomer shift confirmed that the oxidation state of the iron is Fe^{3+}, and the coordination number possibly exists in a distorted FeO_4 tetrahedral and tends to a distorted FeO_6 octahedral [52]. This result agrees with the FTIR and XAENS spectroscopy. The decrease in the quadruple splitting is referred to increase in symmetry around the Fe atom and decreasing the distortion of the FeO_4 where that addition of the Y_2O_3 increases the crystallinity of the structure, which is compatible with the X-ray result, and also from the value of the line width, we can predict that. Considering that decrease in the line width means that the system tends to be crystalline [53].

After heat treatment, as shown in Fig. 11 (b), observed that 1YPVFN continues 1 doublet while the 3YPVFN has two doublets, and the 5PVFN has three doublets; all of this is attributed to Fe^{3+}. Taking into account the doublet attributed to the octahedra, The value of the isomer shift decreased from $0.43_{\pm 0.01}$ to $0.419_{\pm 0.01}$ mm s^{-1} and the value of the quadrupole splitting were observed increasing from $0.32_{\pm 0.01}$ to $0.36_{\pm 0.02}$ mm s^{-1} this led to the increasing in the disorder around the Fe

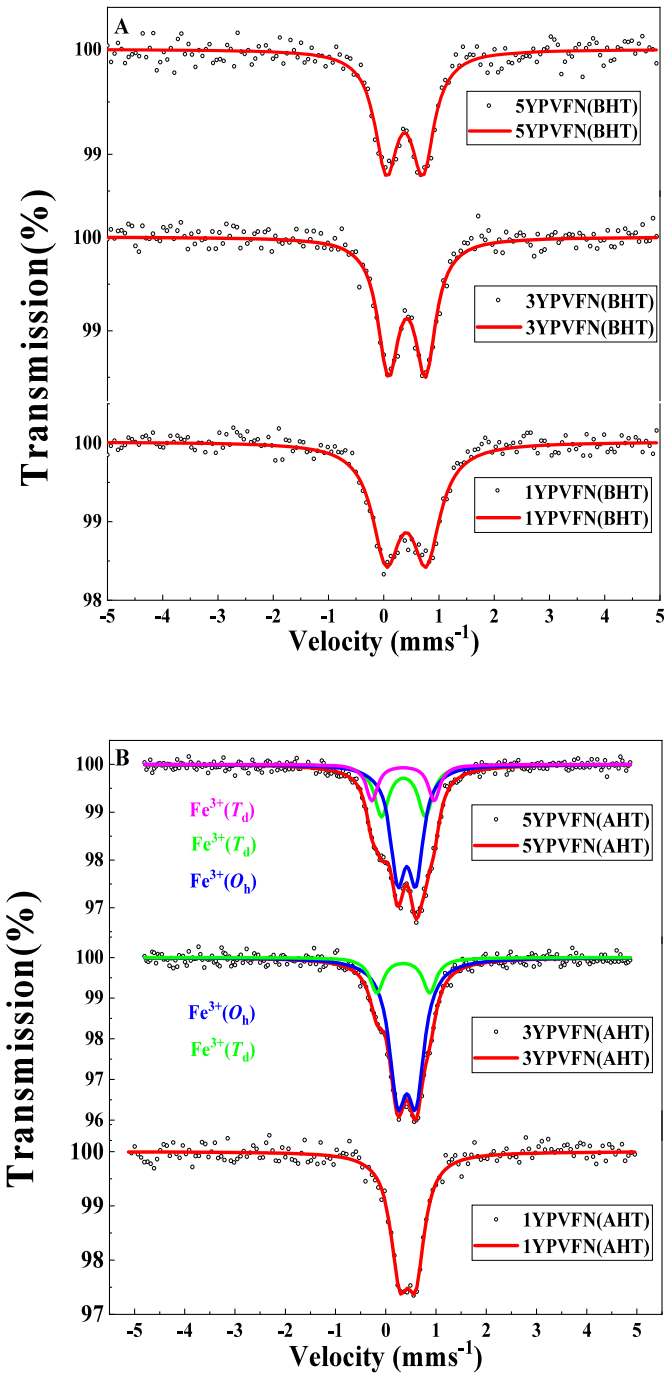

Fig. 11. ^{57}Fe Mössbauer spectra of *x*YPVFN glass-ceramics with *x* of 1, 3 and 5 (A) before and (B) after heat treatment at 500 °C for 100 min.

ions. This is quite clear when seen the value of the absorption area *A*(%) that is decreasing from 100% for 1YPVFN to 57.06% for 5YPVFN, and also from existing of the two doublet for tetrahedral and the area of these two doubles is increasing also when concentration of the Y_2O_3, this was agreement with the XAFX predict. May be this happened due to the change in the structure as confirmed from XRD [51].

3.6. Solid-state impedance spectroscopy (ss-IS)

In analyzing electrical properties, the focus was placed on the trend of DC conductivity and activation energy for DC conductivity, E_{DC}, with the increase of Y_2O_3 concentration, and the changes caused by heat treatment. Fig. 12(a–b) shows conductivity spectra for 1YPVFN before and after heat treatment as representative spectra for all samples in this study. The spectra of the 1YPVFN before heat treatment are characterized by a wide frequency-independent area, i.e. DC plateau, characteristic of electronic conductivity. Next, there is a very small frequency-dependent part of the spectra, so-called conductivity dispersion, which appears only at the lowest temperatures and shifts out of the measurement frequency range as the temperature increases, see Fig. 12(a). In the case of 1YPVFN after heat treatment, the absence of conductivity dispersion is observed in the whole temperature and frequency range, see Fig. 12(b). In addition, the absence of electrode polarization effect at low frequencies and high temperatures further indicates that the nature of the charge transport is electronic rather than ionic. Although samples contain 15 mol% of Na_2O, it seems that the mobility of Na^+ ions is very low, hence the contribution of the ionic conductivity is negligible.

The DC conductivity of all samples increases with increasing temperature, revealing a thermally activated process which follows the Arrhenius behavior [54]. The activation energy for the DC conduction process, E_{DC}, can be determined from the slope of the linear dependence log (σ_{DC}) vs. 1000 T^{-1}/K^{-1}, using the following expression: $\sigma_{DC} = \sigma_0^* \cdot e^{-\frac{E_{DC}}{k_B T}}$, where σ_{DC} is the DC conductivity, σ_0^* is the pre-exponential factor, k_B is the Boltzmann constant, and T is the temperature in K. Table 6 lists the calculated activation energies with other electrical parameters for all samples, BHT and AHT.

From Tables 6 and it can be seen that with the increase in the proportion of Y_2O_3, the DC conductivity of the samples before heat treatment increases, from 2.18×10^{-5} $(\Omega\ cm)^{-1}$ for the 1YPVFN sample up to 1.35×10^{-4} $(\Omega\ cm)^{-1}$ for 5YPVFN. The observed increase in conductivity by factor of 6, Fig. 12(c), is related to the change in the glass composition, see Table 6, and hence changes in the structural features of the glass network, *i.e.*, the addition of Y_2O_3 causes depolymerization of the phosphate network which has a facilitating effect on the formation and transport of polarons (electrons) [54,55].

As stated above, the nature of conductivity is dominantly electronic due to V_2O_5 and its well-known ability to participate in electrical transport owing to the presence of vanadium in multiple oxidation states, which was shown by XANES analysis, see Figs. 9 and 10. With phosphate subnetwork depolymerization, vanadium units are getting in closer proximity, which facilitates and increases the probability of electron hopping between V^{4+} and V^{5+} ions, and results in conductivity increase. Also, Fe ions are known to participate in the transfer of electrons; however, in our case, XANES and Mössbauer spectroscopy showed the presence of only Fe^{3+} ions. Therefore, the polaron conduction *via* Fe ions in different oxidation states can be excluded. However, although Fe^{3+} ions only act structurally by binding NBOs and forming mixed Fe–O–P and Fe–O–V bridges and do not directly contribute to charge transport, such bridges may still facilitate electron hopping through heteronuclear V–O–Fe–O–V linkages.

It is well known that partial crystallization has a strong impact on the electrical conductivity of oxide glasses [56,57]. After heat treatment of *x*YNPVF glasses, in addition to the already present YPO_4 crystalline phase, new crystalline phases appeared, $NaVP_2O_7$ and $Na_{0.282}V_2O_5$, The former phase is typically associated with enhanced Na^+ transport due to its open framework [56,58], while the latter one corresponds to a vanadium bronze phase, known for its mixed-valence states that favors dominant electronic conduction [58]. The coexistence of these phases, therefore, contributes positively to the overall conductivity. Though $NaVP_2O_7$ is expected to induce ionic transport, crystalline $Na_{0.282}V_2O_5$ provides dominant electronic pathways, in addition to a remaining amorphous matrix which strongly favors electronic (polaronic) conductivity. Therefore, the conductivity values of the *x*YNPVF AHT series increased by almost three orders of magnitude, showing the same trend with Y_2O_3 concentration as for the samples BHT, the σ_{DC} value of 1YPVFN and 5YPVFN is 10.6 $(m\Omega\ cm)^{-1}$ and 19.8 $(m\Omega\ cm)^{-1}$ @30 °C, respectively. Also, based on the features of the conductivity spectra, see Fig. 12(b), it can be concluded that electronic transport is dominant,

Table 5
Mössbauer parameters of *x*YPVFN-BHT and AHT.

Concentration (Y) mol %	component	species	BHT ISOMER SHIFT δ (mm s^{-1}	Q. SPLITTING Δ [mm s^{-1}]	LINE. WIDTH Γ [mm s^{-1}]	component	species	AHT ISOMER SHIFT δ [mm s^{-1}]	Q. SPLITTING Δ [mm s^{-1}]	LINE. WIDTH Γ [mm s^{-1}]	Absorption A [%]
1	doublet	Fe^{3+} (O_h)	$0.42_{\pm0.01}$	$0.72_{\pm0.01}$	$0.61_{\pm0.02}$	1st doublet	Fe^{3+} (O_h)	$0.43_{\pm0.01}$	$0.32_{\pm0.01}$	$0.42_{\pm0.02}$	100
3	doublet	Fe^{3+} (T_d)	$0.40_{\pm0.01}$	$0.67_{\pm0.01}$	$0.46_{\pm0.02}$	1st doublet	Fe^{3+} (T_d)	$0.35_{\pm0.01}$	$1.053_{\pm0.01}$	$0.33_{\pm0.04}$	18.53
						2nd doublet	Fe^{3+} (O_h)	$0.420_{\pm0.0034}$	$0.36_{\pm0.008}$	$0.40_{\pm0.017}$	81.47
5	doublet	Fe^{3+} (T_d)	$0.39_{\pm0.01}$	$0.66_{\pm0.02}$	$0.50_{\pm0.02}$	1st doublet	Fe^{3+} (T_d)	$0.35_{\pm0.006}$	$0.87_{\pm0.056}$	$0.35_{\pm0.0.086}$	27.31
						2nd doublet	Fe^{3+} (T_d)	$0.345_{\pm0.007}$	$1.24_{\pm0.005}$	$0.28_{\pm0.06}$	15.63
						3rd doublet	Fe^{3+} (O_h)	$0.419_{\pm0.004}$	$0.36_{\pm0.009}$	$0.36_{\pm0.017}$	57.06

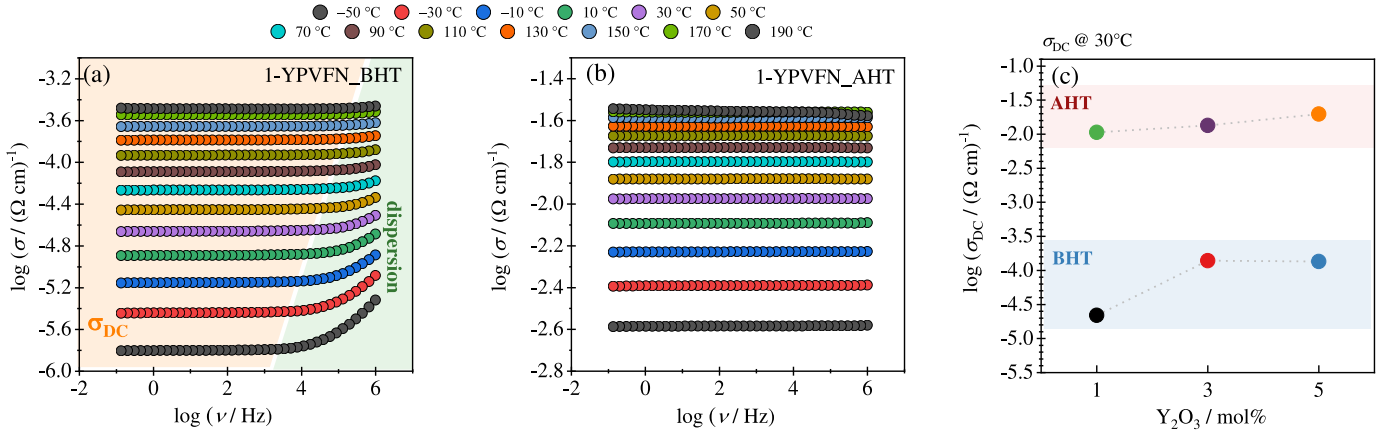

Fig. 12. (a) Conductivity spectra of 1YPVF sample (a) before, BHT, and (b) after heat-treatment, AHT, at 500 °C for 100 min, (c) DC conductivity @30 °C for BHT and AHT samples. The lines in (c) are drawn as guides to the eye.

Table 6
DC conductivity (σ_{DC}), activation energy (E_{DC}), and pre-exponential factor (log σ^*_0) for *x*YPVF BHT and AHT series.

Sample code	BHT			AHT		
	σ^a_{DC} [(Ω cm)$^{-1}$]	E_{DC} [eV]	log σ_0* [(Ω cm)$^{-1}$]	σ^a_{DC} [(Ω cm)$^{-1}$]	E_{DC} [eV]	log σ_0* [(Ω cm)$^{-1}$]
1YPVFN	2.18×10^{-5}	0.20	−1.28	0.0106	0.10	−0.38
3YPVFN	1.38×10^{-4}	0.18	−0.87	0.0134	0.11	−0.12
5YPVFN	1.35×10^{-4}	0.18	−0.91	0.0198	0.10	−0.15

since no signature of electrode polarization due to ionic blocking is observed.

The activation energy for DC conductivity, E_{DC}, exhibits similar correlations to the changes in glass composition and structure. The E_{DC} increased from ~0.18 eV for 5YPVFN to ~0.2 eV for 1YPVFN before heat-treatment. After heat-treatment, the value of E_{DC} decreased even more, to ~0.1 eV for all three samples, confirming that structural reorganization and partial crystallization significantly facilitate charge transport. In both series, BHT and AHT, low E_{DC} values are in line with predominant and rapid electronic transport *via* a small polaron hopping mechanism (SPH) [54,55]. Therefore, the incorporation of Y_2O_3 into the glass matrix and additional crystallization induced by heat-treatment enhances the conductivity and simultaneously lowers the activation energy through (micro)structural modifications.

3.7. Battery performance

Fig. 13(a–f) depicts the charge-discharge curve for a BHT-*x*YNPVF and AHT-*x*YNPVF. During charging and discharge processing, there is no plateau observed where the capacitance increased with a specific voltage. However, there is a difference in capacity between before and after treatment states.

The charge-discharge capacity of BHT-*x*YNPVF, AHT-*x*YNPVF, as a function of Y_2O_3 content, was recorded for 30 cycles, as shown in Fig. 14 (a). The charge-discharge was measured under a current density of 50 mA g^{-1}, and the voltage changed between (0.8 – 4.0) V, The initial discharge capacity for BHT-*x*YNPVF glasses was observed at 20.6, 31.7, 35.2 mAh g^{-1} for 1YPVFN, 3YPVFN, 5YPVFN, respectively and the capacity retention of 1YPVFN, 3YPVFN, 5YPVFN were 31.2%, 25.5%, 29.5%, respectively.

From a different point of view, Fig. 14 (b) shows that the charge-discharge capacity for AHT-*x*YNPVF was measured in 30 cycles. The initial discharge capacities were 57.4, 35.1 and 31 mAh g^{-1} for 1YPVFN, 3YPVFN, and 5YPVFN, respectively. The capacity retention of 1YPVFN, 3YPVFN, and 5YPVFN were 48.4%, 59% and 57.8%, respectively, as listed in Table 7. Fig. 15(a and b) shows the rate of capability of BHT-*x*YNPVF and AHT-*x*YNPVF for glass-ceramics samples in the range 5-200 mAg^{-1}. The initial discharge capacity at 5 mA g^{-1} for BHT-*x*YNPVF glasses was found at 128, 137, and 139 mAh g^{-1} for 1YPVFN, 3YPVFN, and 5YPVFN, respectively, and for *x*YNPVF-AHT the initial discharge capacities at 5 mA g^{-1} were 210, 193, and 153 mAhg^{-1} for

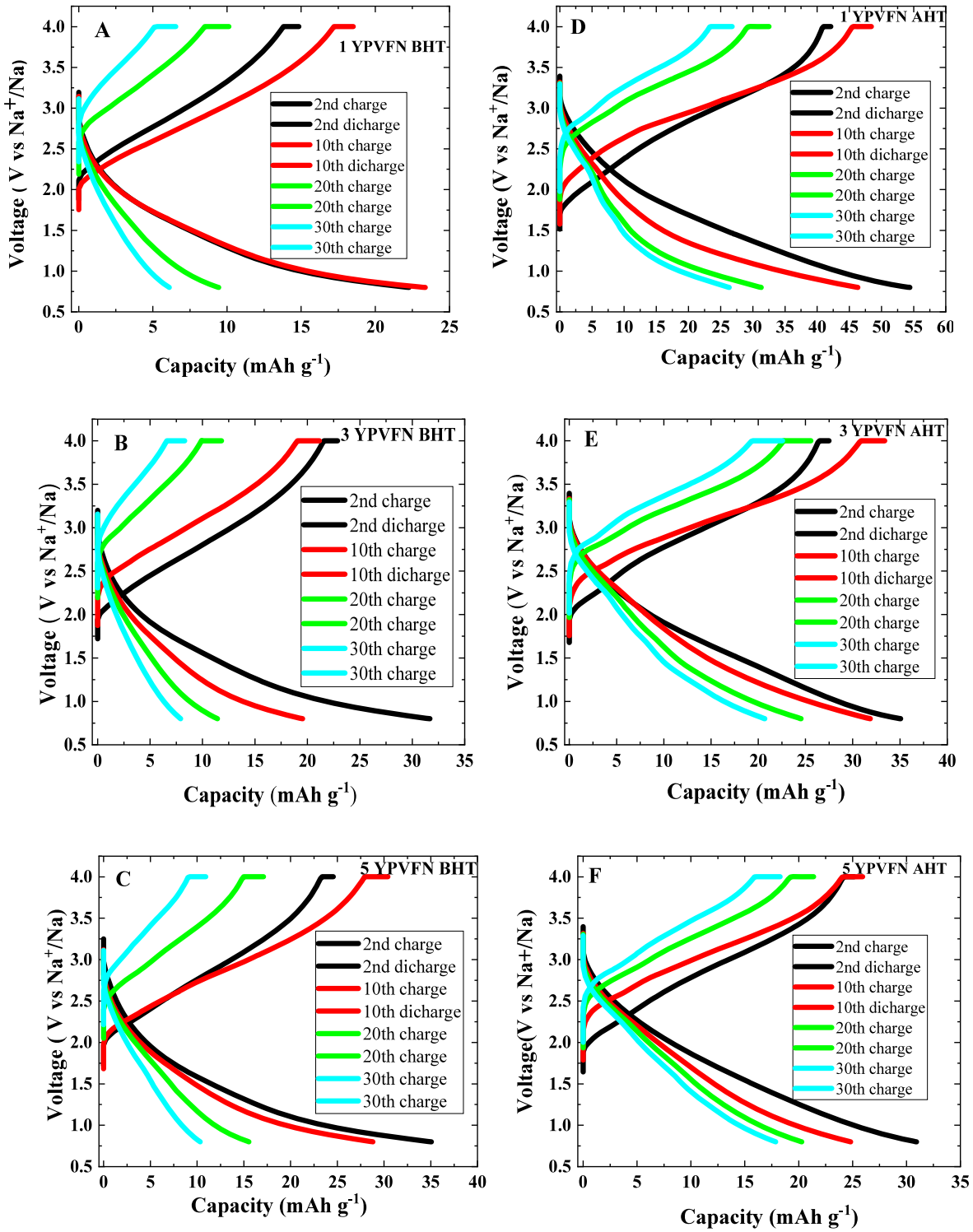

Fig. 13. Charge-discharge curves of *x*YPVFN glass ceramic before and after heat treatment at 500 °C for 100 min, in SIB (A) 1YPVFN (BHT) and (B) 3YPVFN (BHT), (C) 5YPVFN (BHT), (D) 1YPVFN (AHT) and (E) 3YPVFN (AHT), (F) 5YPVFN (AHT).

1YPVFN, 3YPVFN, and 5YPVFN, respectively. It is notable that the highest capacity was recorded for BHT- 5YPVFN and AHT-1YPVFN.

The high capacity of 5YPVFN-BHT can be attributed to its high concentration of Y_2O_3, which promotes an increase in non-bridging oxygen atoms. This leads to the breaking of P-O-P, V-O-V, or both bonds, resulting in an expanded structural distance (i.e., a more open structure) that allows for greater mobility of Na^+ ions. This, in turn, is reflected in the battery performance that leads to an increase in capacity [16,51].

Considering AHT-1YPVFN, there are three precipitated phases: $Na_{0.282}V_2O_5$, YPO_4, and $NaVP_2O_7$. The capacity increases temporarily depending on $Na_{0.282}V_2O_5$, which allows Na^+ to pass through it and improves the intercalation/deintercalation processes because of its flexible structure. When the increase in the concentration of Y_2O_3 leads to an increase in the phase of YPO_4 and a decrease in the percentage of $Na_{0.282}V_2O_5$, as seen from the X-ray results, and since this phase is

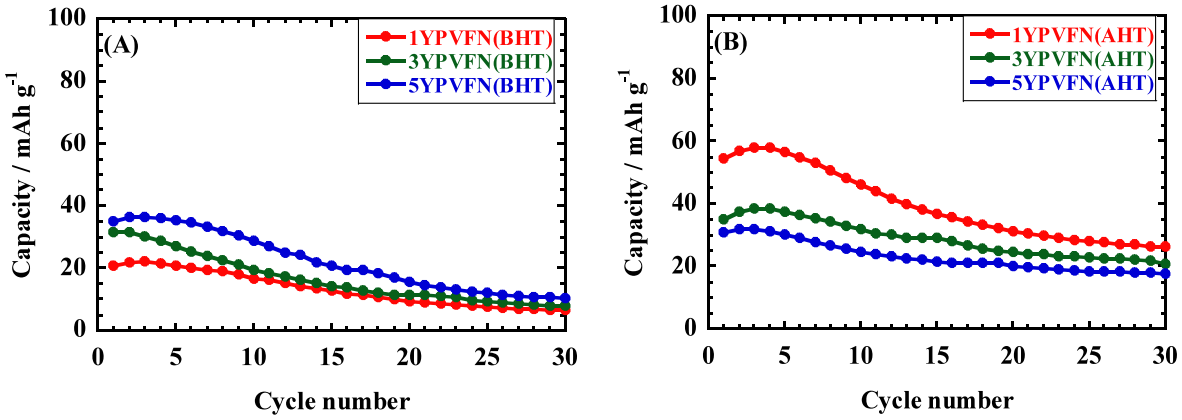

Fig. 14. 30-time recyclability test of the Na-ion battery containing (A) *x*YPVFN before and (B) after heat treatment at 500 °C for 100 min.

Table 7
The discharge capacity and capacity retention (%) of *x*YPVFN-BHT and XYPVF-AHT, measured at 50 mAh g^{-1} for current density in the voltage range of 0.8–4 V.

Name of Sample	BHT		AHT	
	Initial discharge capacity	Capacity retention	Initial discharge capacity	Capacity retention
	[$mAhg^{-1}$]	[%]	[$mAhg^{-1}$]	[%]
1YPVFN	20.7	31.3	57.4	48.4
3YPVFN	31.7	25.0	35.1	59.0
5YPVFN	35.1	29.5	30.9	57.8

classified as an inactive chemical phase, this, in turn, prevents the mobility of Na^+ ions, which decreases the capacity as observed in 3YPVFN-AHT and AHT-5YPVFN compared with AHT-1YPVF.

Also dependent on the XANES and EXAFS result, it was found that demonstrated of V^{5+} and reduced V^{4+} content after heating, which led to limiting the number of redox-active sites [57]. This explains why $NaVP_2O_7$ is not effective, although it is considered one of the phases that influence in the process of intercalation/deintercalation for Na^+ [58, 59].

Table 8 shows that battery performance for 1YPVFN-AHT glass-ceramics cathode with another cathode material that contains oxide transition metal used in sodium-ion batteries as a cathode. Prabeer et al. show that the initial capacity for $Na_2(VO)P_2O_7$ is 80 mAh g^{-1} under a current density 4 mAg^{-1} for 3 cycles used as a cathode for a sodium ion battery, while the initial discharge capacity for the 1YPVFN glass-ceramics at 5 mA for 5 cycles is 210 mAh g^{-1} [60]. Rui et al. used $Na_3V_3(PO_4)_4$ as a cathode for sodium-ion batteries and found that the initial capacity is 37 mAh g^{-1} for 67.5 mA g^{-1}, while 1YPVFN shows 57.4 mAh g^{-1} when the current density is 50 mA [15]. Based on the

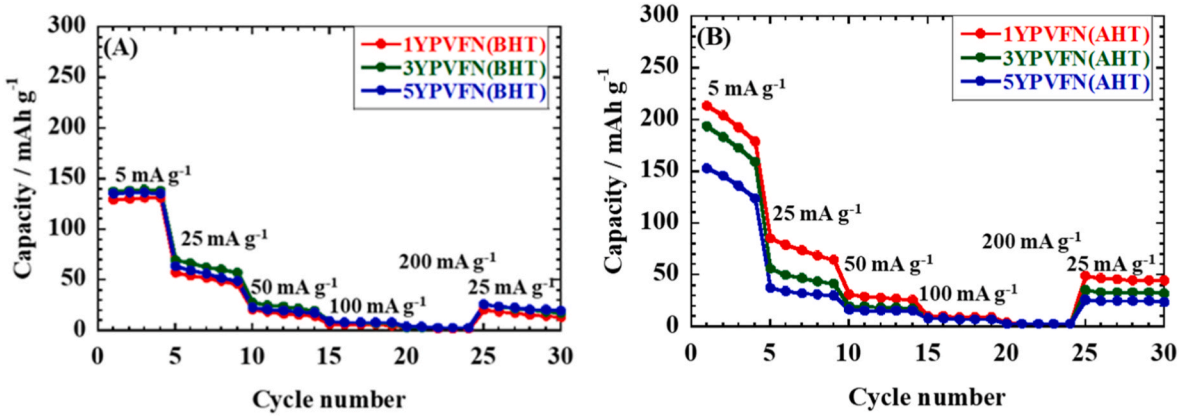

Fig. 15. The rate capability test of the Na-ion battery containing (A) *x*YPVFN before and (B) after heat treatment at 500 °C for 100 min.

Table 8
Comparison of battery performance of PVF -based sodium-ion batteries cathodes.

Material	Voltage range	Specific capacity (mAh g^{-1})	Current density (mA g^{-1})	Capacity retention (%)/(Cycles)	Reference
$Na_3V_3(PO_4)_4$	3-4.4	43	13	(5)	[15]
$Na_2VOP_2O_7$	2-4.5	80	4	(3)	[60]
$Na_2MnP_2O_7$	2–4.5	36	10	80 (3)	[61]
$Na_2Fe_{0.25}Ni_{0.75}P_2O_7$	2–5	21.8	10	60(15)	[62]
$FePO_4$	2.5-4.2	40	40	80(50)	[63]
$Na_7V_4(P_2O_7)_4(PO_4)$	2-4	86	46	81.4 (300)	[64]
$NaV(PO_4)_2F_2$	2-4	61	6.1		[65]
1YPVFN-AHT	0.8-4	210	5	30	This work
	0.8-4	57	50	30	This work

above results and the data presented in Table 7, the 1YPVFN glass-ceramic has promising characteristics for application as a cathode material in sodium-ion batteries (SIBs).

4. Conclusion

PVF glass ceramics doped with Y_2O_3 were successfully prepared. The structural and electrical electrochemical properties of this glass system were investigated. DTA and X-ray showed that the prepared sample has an amorphous phase. The X-ray confirms the nanoscale of the prepared system in the state before and after heat treatment, after calculating the particle size by using the Scherrer equation. After heat treatment, the X-Ray shows that perception for the three crystalline phases YPO_4 and $NaVP_2O_7$, and $Na_{0.282}V_2O_5$. FTIR results for BHT and AHT show that an increase in the Y_2O_3 led to an increase in NBO. The Mössbauer spectrum for BHT shows Isomer shift δ and quadrupole splitting Δ decrease with increasing Y_2O_3 the oxidation state of the iron is Fe^{3+}. AHT shows Isomer shift δ decreased and the quadrupole splitting Δ increases with increasing Y_2O_3 and the oxidation state of the iron Fe^{3+}. The XANES and EXAFS for the Fe show that the oxidation state of the iron in the tetrahedral state Fe^{3+} increases in the Y_2O_3 no significant impact on its oxidation state before and after heat treatment, in agreement with the Mössbauer result. With respect to vanadium, show dominance the V^{5+} in structure in BHT and AHT for all samples. The incorporation of Y_2O_3 into vanadium-phosphate based glasses improves the electrical conductivity and lowers the activation energy due to induced structural changes. Furthermore, partial crystallization upon heat treatment leads to the formation of vanadium-rich phases, resulting in an additional increase in DC conductivity and a decrease on activation energies as down to ~0.1 eV, confirming the strong impact of controlled nano structuring on charge transport. The best battery performance is shown at AHT -1YPVFN glass-ceramics, where the initial discharge capacity is 210 mAh g^{-1} at 5 mA g^{-1} and 57.4 mAh g^{-1} when the current density is 50 mA g^{-1}, which suggests that the AHT-1YPVFNhas promising characteristics for application as a cathode material in sodium-ion batteries (SIBs). According to these results, our expectation of enhancing the capacity of PVF glass by adding Y_2O_3 has been achieved.

CRediT authorship contribution statement

A. Shreif: Writing – original draft, Visualization, Validation, Methodology, Formal analysis, Data curation, Conceptualization. **Y. Arita:** Software, Methodology, Data curation. **Z. Homonnay:** Writing – review & editing. **E. Kuzmann:** Writing – review & editing. **M. Kudor:** Writing – review & editing. **K.A. Beres:** Writing – review & editing. **S. Krehula:** Writing – review & editing. **M. Marciuš:** Writing – review & editing. **L. Pavić:** Writing – review & editing, Software, Data curation. **A. Šantić:** Writing – review & editing. **M. Razum:** Writing – review & editing. **S. Kubuki:** Writing – original draft, Supervision, Project administration, Methodology, Conceptualization.

Declaration of competing interest

The authors declare that they have no known competing financial interests or personal relationships that could have appeared to influence the work reported in this paper.

Acknowledgement

This work was supported by JSPS KAKENHI (Grant No. 23K26763). The authors also acknowledge the support of the Tokyo Metropolitan Government.

Appendix A. Supplementary data

Supplementary data to this article can be found online at https://doi.org/10.1016/j.ceramint.2026.02.289.

References

[1] T. Martins, A.C. Barreto, F.M. Souza, A.M. Souza, Fossil fuels consumption and carbon dioxide emissions in G7 countries: empirical evidence from ARDL bounds testing approach, Environ. Pollut. 291 (2021) 118093, https://doi.org/10.1016/j.envpol.2021.118093.
[2] M. Filonchyka, M.P. Petersond, L. Zhanga, V. Hurynovicha, Y. Hea, Greenhouse gases emissions and global climate change: examining the influence of CO_2, CH_4, and N_2O, Sci. Total Environ. 935 (2024) 173359, https://doi.org/10.1016/j.scitotenv.2024.173359.
[3] T.Z. Ang, M. Salem, M. Kamarol, H.S. Das, M.A. Nazari, N. Prabaharan, A comprehensive study of renewable energy sources: classifications, challenges and suggestions, Energy Strategy Rev. 43 (2022) 100939, https://doi.org/10.1016/j.esr.2022.100939.
[4] H.A. Ibrahim, M.K. Ayomoh, M.N. Gitau, S.S. Venkatta, R.C. Bansal, R. Naidoo, Sustainability of power generation for developing economies: a systematic review of power sources mix, Energy Strategy Rev. 47 (2023) 101085, https://doi.org/10.1016/j.esr.2023.101085.
[5] A. Osman, L. Chen, M. Yung, G. Msigwa, M. Farghali, D. Rooney, P. Yap, S. Fawsy, Environmental impact and resilience of renewable energy under a changing climate: a review, Environ. Chem. Lett. 21 (2023) 741–764, https://doi.org/10.1007/s10311-022-01532-8.
[6] M. Schauf, S. Schwenen, System price dynamics for battery storage, Energy Policy 183 (2023) 113836, https://doi.org/10.1016/j.enpol.2023.113836.
[7] J. Hoppmann, J. Volland, T. Schmidt, V. Hoffmann, The economic viability of battery storage for residential solar photovoltaic systems-A review and a simulation model, Renew. Sustain. Energy Rev. 39 (2014) 1101–1118, https://doi.org/10.1016/j.rser.2014.07.068.
[8] N. Chatzigeorgiou, S. Theocharides, G. Makrides, G. Georghiou, A review on battery energy storage systems: applications, developments, and research trends of hybrid installations in the end-user sector, J. Energy Storage 86 (2024) 111192, https://doi.org/10.1016/j.est.2024.111192.
[9] E. Enasel, G. Dumitrascu, Storage solutions for renewable energy: a review, Energy Nexus 17 (2025) 100391, https://doi.org/10.1016/j.nexus.2025.100391.
[10] Y. Wang, Y. Wang, Y.-X. Wang, X. Feng, W. Chen, X. Ai, H. Yang, Y. Cao, Developments and perspectives on emerging high-energy-density sodium-metal batteries, Chem 5 (2019) 2547–2570, https://doi.org/10.1016/j.chempr.2019.05.026.
[11] S. Marijan, T. Klaser, M. Mirosavljević, P. Mošner, L. Koudelka, Ž. Skoko, J. Pisk, L. Pavić, Exploring the effect of V_2O_5 and Nb_2O_5 content on the structural, thermal, and electrical characteristics of sodium phosphate glasses and glass-ceramics, Int. J. Mol. Sci. 25 (2024) 3005, https://doi.org/10.3390/ijms2505300.
[12] Zihan Wang, Shao-hua Luoa, Xian Zhanga, Song Guo, Pengwei Lia, Shengxue Yan, Glass and glass ceramic electrodes and solid electrolyte materials for lithium ion batteries: a review, J. Non-Cryst. Solids 619 (2023) 122581, https://doi.org/10.1016/j.jnoncrysol.2023.122581.
[13] H. Yang, D. Wang, Y. Liu, Y. Liu, B. Zhong, Y. Song, Q. Kong, Z. Wu, X. Guo, Improvement of cycle life for layered oxide cathodes in sodium-ion batteries, Energy Environ. Sci. 17 (2024) 1756–1780, https://doi.org/10.1039/D3EE02934D.
[14] S. Kubuki, K. Osouda, A.S. Ali, I. Khan, B. Zhang, A. Kitajou, S. Okada, J. Okabayashi, Z. Homonnay, E. Kuzmann, T. Nishida, L. Pavić, A. Šantić, A. Moguš-Milanković, ^{57}Fe-Mössbauer and XAFS studies of conductive sodium phospho-vanadate glass as a cathode active material for Na-ion batteries with large capacity, J. Non-Cryst. Solids 570 (2021) 120998, https://doi.org/10.1016/j.jnoncrysol.2021.120998.
[15] R. Liu, H. Liu, T. Sheng, S. Zheng, G. Zhong, G. Zheng, Z. Liang, G.F. Ortiz, W. Zhao, J. Mi, Y. Yang, Novel 3.9 V layered $Na_3V_3(PO_4)_4$ cathode material for sodium ion batteries, ACS Appl. Energy Mater. 1 (2018) 3603–3606, https://doi.org/10.1021/acsaem.8b00889.
[16] A. Arafat, S.A. Samad, J.J. Titman, A.L. Lewis, E.R. Barney, I. Ahmed, Yttrium doped phosphate-based glasses: structural and degradation analyses, Biomed. Glasses 6 (2020) 34–49, https://doi.org/10.1515/bglass-2020-0004.
[17] G.V. Nechaev, S.G. Vlasova, O.G. Reznitskikh, Conductivity in sodium-yttrium-silicate and sodium-yttrium-phosphate glass, Glass Phys. Chem. 41 (2015) 64–67, https://doi.org/10.1134/S1087659615010174.
[18] S. Wang, K. Liang, H. Zhao, M. Wu, J. He, P. Wei, Z. Ding, J. Li, X. Huang, Y. Ren, Electronic structure formed by Y_2O_3-doping in lithium position assists improvement of charging-voltage for high-nickel cathodes, Nat. Commun. 16 (2025) 1, https://doi.org/10.1038/s41467-024-52768-7.
[19] N. Li, R. An, Y. Su, F. Wu, L. B, L. Chen, Y. Zheng, H. Shoua, S. Chen, The role of yttrium content in improving electrochemical performance of layered lithium-rich cathode materials for Li-ion batteries, J. Mater. Chem. A 34 (2013), https://doi.org/10.1039/C3TA11665D.
[20] S. Ziraki, M. Kanani, B. Hashemi, M.M. Loghavi, Effect of sodium and yttrium co-doping on electrochemical performance of $LiNi_{0.8}Co_{0.15}Al_{0.05}O_2$ cathode material for Li-ion batteries: computational and experimental investigation, J. Energy Storage 70 (2023) 107983, https://doi.org/10.1016/j.est.2023.107983.
[21] J. Chen, X. Wang, Z. Ma, G. Shao, Effects of yttrium ion doping on electrochemical performance of $LiFePO_4$/C cathodes for lithium-ion battery, Ionics 21 (2015) 2701–2708, https://doi.org/10.1007/s11581-015-1467-2.

[22] A.A. Bahgat, M.G. Moustafa, E.E. Shaisha, Enhancement of electric conductivity in transparent glass-ceramic nanocomposites of Bi_2O_3-$BaTiO_3$ glasses, J. Mater. Sci. Technol. 29 (12) (2013) 1166–1176, https://doi.org/10.1016/j.jmst.2013.08.005.

[23] D.D. Thornburg, Evaluation of glass formation tendency from rate dependent thermograms, Mater. Res. Bull. 9 (1974) 1481–1486, https://doi.org/10.1016/0025-5408(74)90094-4.

[24] J.S.J. Hargreaves, Some considerations related to the use of the Scherrer equation in powder X-ray diffraction as applied to heterogeneous catalysts, Catal. Struct. React. 2 (2016) 33–37, https://doi.org/10.1080/2055074X.2016.1252548.

[25] Y. Cai, J. Zhou, G. Fang, G. Cai, A. Pan, S. Liang, $Na_{0.282}V_2O_5$: a high-performance cathode material for rechargeable lithium batteries and sodium batteries, J. Power Sources 328 (2016) 241–249, https://doi.org/10.1016/j.jpowsour.2016.08.016.

[26] J.R. Van Wazer, The Phosphorous and its Compounds, vols. 1 and 2, Interscience, New York, 1951.

[27] Y.M. Moustafa, K. El-Egili, Infrared spectra of sodium phosphate glasses, J. Non-Cryst. Solids 240 (1998) 144–153, https://doi.org/10.1016/S0022-3093(98)00711-X.

[28] A. Ibrahim, Y. Arita, A.S. Ali, I. Khan, B. Zhang, M. Razum, L. Pavić, A. Santić, Z. Homonnay, E. Kuzmann, M.Y. Hassaan, J. Wang, S. Kubuki, Impact of adding Fe ions on the local structure and electrochemical performance of P_2O_5-V_2O_5 glass and glass ceramics used as a cathode in LIBs, J. Phys. Chem. Solid. 179 (2023) 111391, https://doi.org/10.1016/j.jpcs.2023.111391.

[29] M.A. Farag, A. Ibrahim, M.Y. Hassaan, Enhancement of structural and optical properties of transparent sodium zinc phosphate glass–ceramics nanocomposite, J. Australas. Ceram. Soc. 58 (2022) 653–661, https://doi.org/10.1007/s41779-022-00716-3.

[30] R. Balaji Rao, N.O. Gopal, N. Veeraiah, Studies on the influence of V_2O_5 on dielectric relaxation and ac conduction phenomena of Li_2O-MgO-B_2O_3 glass system, J. Alloys Compd. 368 (2004) 25–37, https://doi.org/10.1016/j.jallcom.2003.08.07.

[31] M.Y. Hassaan, M.G. Moustafa, K. Osouda, S. Kubuki, T. Nishida, ^{57}Fe and ^{119}Sn Mössbauer, XRD, FTIR and DC conductivity study of Li_2O-Fe_2O_3-SnO_2-P_2O_5 glass and glass ceramics, J. Alloys Compd. 765 (2018) 121–127, https://doi.org/10.1016/j.jallcom.2018.06.207.

[32] N. Laorodphan, P. Pooddee, P. Kidkhunthod, P. Kunthadee, W. Tapala, R. Puntharod, Boron and pentavalent vanadium local environments in binary vanadium borate glasses, J. Non-Cryst. Solids 453 (2016) 118–124, https://doi.org/10.1016/j.jnoncrysol.2016.10.005.

[33] J. Mohapatr, A. Mitra, H. Tyagi, D. Bahadur, M. Aslam, Iron oxide nanorods as high-performance magnetic resonance imaging contrast agents, Nanoscale 7 (2015) 9174–9184, https://doi.org/10.1039/c5nr00055f.

[34] N.O. Dantas, W.E.F. Ayta, A.C.A. Silva, N.F. Cano, S.W. Silva, P.C. Morais, Effect of Fe_2O_3 concentration on the structure of the SiO_2-Na_2O-Al_2O_3-B_2O_3 glass system, Spectrochim. Acta, Part A 81 (2011) 140–143, https://doi.org/10.1016/j.saa.2011.05.074.

[35] L. Srinivasa Rao, M. Srinivasa Reddy, M. Rami Reddy, N. Veeraiah, Dielectric dispersion in Li_2O-MoO_3-B_2O_3 glass system doped with V_2O_5, J. Alloys Compd. 464 (2008) 472–482, https://doi.org/10.1016/j.jallcom.2007.10.016.

[36] Zhuangzhi Li, Lang Qiu, Ping Li, Hao Liu, Dong Wang, Weibo Hua, Ting Chen, Yang Song, Wan Fang, Benhe Zhong, Zhenguo Wu, Xiaodong Gu, Exposing the (002) active facet by reducing surface energy for a high-performance $Na_3V_2(PO_4)_2F_3$ cathode, J. Mater. Chem. A 12 (2024) 7777–7787, https://doi.org/10.1039/d3ta07954f.

[37] K. Matsuda, S. Kubuki, K. Akiyama, Z. Homonnay, K. Sinko, E. Kuzmann, T. Nishida, A relationship between electrical conductivity and structural relaxation of $10SnO_2$·$10Fe_2O_3$·$10P_2O_5$·xAgI·$(70\text{-}x)V_2O_5$ glass caused by heat-treatment, J. Ceram. Soc. Japan 123 (2015) 121–128, https://doi.org/10.2109/jcersj2.123.121.

[38] L.Y. Zhang, H. Li, L.L. Hu, Statistical structure analysis of GeO_2 modified Yb^{3+}: phosphate glasses based on Raman and FTIR study, J. Alloys Compd. 698 (2017) 103–113, https://doi.org/10.1016/j.jallcom.2016.12.175;

[38b] J. Zhu, Z. Zeng, W.-X. Li, K Edge XANES investigation of Fe-based oxides by density functional theory calculations, J. Phys. Chem. C 125 (2021) 26229–26239, https://doi.org/10.1021/acs.jpcc.1c08461;

[38c] A. Ibrahima, M. Razum, L. Pavić, Z. Homonnay, E. Kuzmann, A. Santić, M. Y. Hassaan, K. Akiyama, S. Kubuki, Enhancing cyclability of Fe_2O_3-V_2O_5-P_2O_5 ceramic cathode for high-performance sodium-ion batteries through heat treatment, Mater. Chem. Phys. 332 (2025) 130231, https://doi.org/10.1016/j.matchemphys.2024.130231.

[39] X. Sun, A. Tayal, A. Ullrich, O. Petracic, S. Haas, Phase composition of iron oxide nanoparticles studied using hard X-ray absorption spectroscopy, J. Phys. Chem. C 127 (2023) 12077–12083, https://doi.org/10.1021/acs.jpcc.3c01023.

[40] T.E. Westre, P.K. Pohl, J.G. DeWitt, B. Hedman, K.O. Hodgson, E.I. Solomon, A multiplet analysis of Fe K-edge 1s - 3d pre-edge features of iron complexes, J. Am. Chem. Soc. 119 (1997) 6297–6314, https://doi.org/10.1021/ja964352a.

[41] T. Aoyagi, T. Fujieda, T. Toyama, K. Kono, D. Takamatsu, T. Hirano, T. Naito, Y. Hayashi, H. Takizawa, Electrochemical properties and in-situ XAFS observation of Li_2O-V_2O_5-P_2O_5-Fe_2O_3 quaternary-glass and crystallized-glass cathodes, J. Non-Cryst. Solids 453 (2016) 28–35, https://doi.org/10.1016/j.jnoncrysol.2016.09.016.

[42] G.A. Horrocks, E.J. Braham, Y. Liang, L.R. De Jesus, J. Jude, J.M. Velazquez, D. Prendergast, S. Banerjee, Vanadium K edge X-ray absorption spectroscopy as a probe of the heterogeneous lithiation of V_2O_5: first principles modelling and principal component analysis, J. Phys. Chem. C 120 (2016) 23922–23932, https://doi.org/10.1021/acs.jpcc.6b06499.

[43] F. He, J. Kang, R. Wang, Z. Li, H. Li, B. Zhong, F. Wan, Z. Wu, X. Guo, Rapid and efficient microwave-assisted solid-phase synthesis of $Na_3V_2(PO_4)_2F_3$ and exploration of the synthesis process, Chem. Commun. 61 (2025) 6623–6626, https://doi.org/10.1039/D5CC01231G.

[44] Z. Li, Y. Wang, H. Hu, L. Qiu, Y. Xiao, L. Li, Z. Wu, X. Guo, Synchronous carbonization and phase-formation via flash Joule heating for uniform carbon-coated polyanionic cathode materials, Adv. Energy Mater. 15 (2025) e03894, https://doi.org/10.1002/aenm.202503894.

[45] F.M.F. de Groot, High-Resolution X-ray emission and X-ray absorption spectroscopy, Chem. Rev. 101 (2001) 1779–1808, https://doi.org/10.1021/cr9900681.

[46] P. Chaurand, J. Rose, V. Briois, M. Salome, O. Proux, V. Nassif, L. Olivi, J. Susini, J.-L. Hazemann, J.-Y. Bottero, New methodological approach for the vanadium K-edge X-ray absorption near-edge structure interpretation: application to the speciation of vanadium in oxide phases from steel slag, J. Phys. Chem. B 111 (2007) 5101–5110, https://doi.org/10.1021/jp063186i.

[47] T. Aoyagi, S. Kohara, T. Naito, Y. Onoder, M. Kodama, T. Onodera, D. Takamatsu, S. Tahara, O. Sakata, T. Miyake, K. Suzuya, K. Ohara, T. Usuki, Y. Hayashi, H. Takizawa, Controlling oxygen coordination and valence of network-forming cations, Sci. Rep. 10 (2020) 7178, https://doi.org/10.1038/s41598-020-63786-y.

[48] J. Wong, F.W. Lytle, R.P. Messmer, D.H. Maylotte, Phys. Rev. B 30 (1984) 5596–5610, https://doi.org/10.1103/PhysRevB.30.5596.

[49] Z. Feng, Q. Ma, H. Feng, J.W. Elam, P.C. Stair, M.J. Bedzyk, Atomic-scale cation dynamics in a monolayer VOX/α-Fe_2O_3 catalyst, RSC Adv. 5 (2015) 103834–103840, https://doi.org/10.1039/c5ra18404e.

[50] A.N. Mansoura, P.H. Smith, W.M. Baker, M. Balasubramanian, J. McBreen, In situ XAS investigation of the oxidation state and local structure of vanadium in discharged and charged V_2O_5 aerogel cathodes, Electrochemical Acta 47 (2002) 3151–3161, https://doi.org/10.1016/S0013-4686(02)00234-7.

[51] T. Nishida, A review of structural studies of superionic conducting borate and semiconducting vanadate glasses by Mössbauer spectroscopy and DTA, J. Non-Cryst. Solids 108 (1989) 87–98, https://doi.org/10.1016/0022-3093(89)90336-0.

[52] T. Nishida, I. Furumoto, Y. Fujita, Structural relaxation and electrical conductivity of molybdovanadate glass, J. Mater. Sci. Mater. Electron. 29 (2018) 2654–2659, https://doi.org/10.1007/s10854-017-8191-9.

[53] H. Kurimoto, T. Nishida, S. Okada, J. Yamaki, ^{57}Fe Mössbauer and DTA study of R_2O·2FeO·V_2O_5·P_2O_5 glasses (R = Li, Na), J. Ceram. Soc. Jpn. 116 (5) (2008) 637–640, https://doi.org/10.2109/jcersj2.116.637.

[54] Mott & Davis, Electronic Processes in Non-crystalline Materials, 1979.

[55] J.E. Garbarczyk, P. Jozwiak, M. Wasiucionek, J.L. Nowinski, Effect of nano crystallization on the electronic conductivity of vanadate–phosphate glasses, Solid State Ionics 177 (26-32) (2006) 2585–2588, https://doi.org/10.1016/j.ssi.2006.04.038.

[56] M.G. Moustafa, Hatem M.H. Saad, M.H. Ammar, Insight on the weak hopping conduction produced by titanium ions in the lead borate glassy system, Mater. Res. Bull. 140 (2021) 111323, https://doi.org/10.1016/j.materresbull.2021.111323.

[57] Oleg A. Drozhzhin, Ilya V. Tertov, Anastasia M. Alekseeva, Dmitry A. Aksyonov, Keith J. Stevenson, Artem M. Abakumov, Evgeny V. Antipov, β-$NaVP_2O_7$ as a superior electrode material for Na-ion batteries, Chem. Mater. 31 (18) (2019) 7463–7469, https://doi.org/10.26434/chemrxiv.8204654.v1.

[58] Hang Zhou, Yongb Lyu, Xin Chengc, Aic Guo, Zhaod Xiaochen, Lijia Tonge, Tingting Xuf, Wenfeng Mao, Partial cationic exchange boosting sodium storage of $NaVP_2O_7$, J. Energy Storage 93 (2024) 112358, https://doi.org/10.1016/j.est.2024.112358.

[59] V.G. Nazin, L.L. Lev, V.A. Rogalev, D.V. Vyalykh, O. Yu Vilkov, D.V. Kapustin, A. A. Bush, V.I. Kapustin, Study of the electronic structure of sodium-vanadium bronze (Na x V_2O_5) single crystals at x = 0.23, 0.28, and 0.33, J. Surf. Investig (8) (2014) 117–126, https://doi.org/10.1134/S1027451014010339.

[60] P. Barpanda, P. Liu, G. Avdeev, M. Yamada, A. t-Na, VO)P_2O_7: a 3.8 V pyrophosphate insertion material for sodium-ion batteries, Chemelectrochem 1 (2014) 1488–1491, https://doi.org/10.1002/cec.201402095.

[61] M. Tanabe, T. Honma, T. Komatsu, Unique crystallization behaviour of sodium manganese pyrophosphate $Na_2MnP_2O_7$ glass and its electrochemical properties, J. Asian Ceram. Soc. 5 (2017) 209–215, https://doi.org/10.1016/j.jascer.2017.04.009.

[62] Y. Ji, T. Honma, T. Komatsu, Crystallization of the $Na_2Fe_xNi_{1-x}P_2O_7$ glass and ability of cathode for sodium-ion batteries, Front. Mater. 7 (2020) 34, https://doi.org/10.3389/fmats.2020.00034.

[63] S.Y. Duan, J.Y. Piao, T.Q. Zhang, Y.G. Sun, X.C. Liu, A.M. Cao, L.J. Wan, Kinetically controlled formation of uniform $FePO_4$ shells and their potential for use in high-performance sodium-ion batteries, NPG Asia Mater. 9 (2017) 414, https://doi.org/10.1038/am.2017.136.

[64] W. Fang, Z. An, J. Xu, H. Zhao, J. Zhang, Superior performance of $Na_7V_4(P_2O_7)_4PO_4$ in sodium-ion batteries, RSC Adv. 8 (2018) 21224–21228, https://doi.org/10.1039/C8RA03682A.

[65] Z. Liang, X. Liu, R. Ortiz, G.F. Zhong, G. Xiang, Y. Chen, S. Mi, J. Wu, S. Yang, New dimorphs of $Na_5V(PO_4)_2F_2$ as an ultrastable cathode material for sodium-ion batteries, ACS Appl. Energy Mater. 3 (2020) 1181–1189, https://doi.org/10.1021/acsaem.9b02248.